SANDIA REPORT

SAND2014-3606
Unlimited Release
Printed June 24, 2014

The Mechanics of Pressed-Pellet Separators in Molten Salt Batteries

Kevin N. Long, Christine C. Roberts, Scott A. Roberts, Anne M. Grillet

Prepared by
Sandia National Laboratories
Albuquerque, New Mexico 87185 and Livermore, California 94550

Sandia National Laboratories is a multi-program laboratory managed and operated by Sandia Corporation, a wholly owned subsidiary of Lockheed Martin Corporation, for the U.S. Department of Energy's National Nuclear Security Administration under contract DE-AC04-94AL85000.

Sandia National Laboratories

Issued by Sandia National Laboratories, operated for the United States Department of Energy by Sandia Corporation.

Available to DOE and DOE contractors from
U.S. Department of Energy
Office of Scientific and Technical Information
P.O. Box 62
Oak Ridge, TN 37831

Telephone: (865) 576-8401
Facsimile: (865) 576-5728
E-Mail: reports@adonis.osti.gov
Online ordering: http://www.osti.gov/bridge

Available to the public from
U.S. Department of Commerce
National Technical Information Service
5285 Port Royal Rd
Springfield, VA 22161

Telephone: (800) 553-6847
Facsimile: (703) 605-6900
E-Mail: orders@ntis.fedworld.gov
Online ordering: http://www.ntis.gov/help/ordermethods.asp?loc=7-4-0#online

SAND2014-3606
Unlimited Release
Printed June 24, 2014

The Mechanics of Pressed-Pellet Separators in Molten Salt Batteries

Kevin N. Long, Christine C. Roberts, Scott A. Roberts, Anne M. Grillet
Engineering Sciences
Sandia National Laboratories
P.O. Box 5800
Albuquerque, NM 87185

Abstract

We present a phenomenological constitutive model that describes the macroscopic behavior of pressed-pellet materials used in molten salt batteries. Such materials include separators, cathodes, and anodes. The purpose of this model is to describe the inelastic deformation associated with the melting of a key constituent, the electrolyte. At room temperature, all constituents of these materials are solid and do not transport cations so that the battery is inert. As the battery is heated, the electrolyte, a constituent typically present in the separator and cathode, melts and conducts charge by flowing through the solid skeletons of the anode, cathode, and separator. The electrochemical circuit is closed in this hot state of the battery.

The focus of this report is on the thermal-mechanical behavior of the separator, which typically exhibits the most deformation of the three pellets during the process of activating a molten salt battery. Separator materials are composed of a compressed mixture of a powdered electrolyte, an inert binder phase, and void space. When the electrolyte melts, macroscopically one observes both a change in volume and shape of the separator that depends on the applied boundary conditions during the melt transition. Although porous flow plays a critical role in the battery mechanics and electrochemistry, the focus of this report is on separator behavior under flow-free conditions in which the total mass of electrolyte is static within the pellet. Specific poromechanics effects such as capillary pressure, pressure-saturation, and electrolyte transport between layers are not considered. Instead, a phenomenological model is presented to describe all such behaviors including the

melting transition of the electrolyte, loss of void space, and isochoric plasticity associated with the binder phase rearrangement. The model is appropriate for use finite element analysis under finite deformation and finite temperature change conditions. The model reasonably describes the stress dependent volume and shape change associated with dead load compression and spring-type boundary conditions; the latter is relevant in molten salt batteries. Future work will transition the model towards describing the solid skeleton of the separator in the traditional poromechanics context.

Acknowledgment

The authors thank William Scherzinger and Benjamin Reedlun for valuable discussions regarding theoretical and numerical considerations of the modeling work appearing in this report and for the use of Benjamin Reedlun's plotting software. We are grateful for the technical reviews provided by Pania Newell and Waiching Sun, which helped shape the conclusions of this paper and the direction of future work.

Contents

Appendix

List of Figures

List of Tables

Chapter 1

Introduction

Molten salt batteries are electrochemical cells that are open circuit below the melting temperature of the electrolyte but readily deliver power above this transition. These batteries typically consist of multiple electrochemical cells stacked like pancakes into a cylinder and packaged under both axial and radial closing forces. In each cell, an anode and cathode are separated by a separator material composed of a powdered oxide and eutectic salt that are compressed together. A procedure for manufacturing separator pellets is described in reference [14]. The multi-phase microstructure of the separator material includes a sizable void fraction of approximately 25% by volume initially due to the manufacturing process [16]. In the cold state of the battery, the electrolyte is solid, and the separator cannot transport cations, but when the electrolyte is in its molten state, cation transport readily occurs. In this report, we will focus on separators composed of 18% by volume MgO binder, 57% by volume eutectic mixture of LiCl-KCl electrolyte, and 25% by volume void space. The melting temperature of the electrolyte is 352 C [12, 16].

As the electrolyte melts, several processes occur simultaneously at the microscale:

- The specific volume of the LiCl-KCl electrolyte expands by 20% in the liquid state relative to the solid state [14]
- The void space is observed to diminish substantially as capillary pressure drives the removal of free surface area
- The particles in the binder phase rearrange until they form a percolated network capable of supporting shear stress. Macroscopically, inelastic shape change is observed during this process.

Macroscopically, these processes result in both volumetric and isochoric (constant volume) shape change of the separator pellets, the details of which are important to the electrochemical performance of the cell. Too much plastic deformation can cause intracell shorting to occur if the anode and cathode pellets come into contact. Alternatively, too much plastic deformation may cause the electrolyte to leak out of the separator material and form an ion conduction pathway through the surrounding insulation leading to intercell parasitic currents [10]. In contrast, if the deformation is too small, there may be poor interfacial contact and inadequate wetting of the separator-cathode and separator-anode interfaces, which would result in a higher internal resistance in the battery [10]. Similar arguments/concerns apply to changing the volume fractions of the electrolyte and

binder phases [14]. For molten salt batteries, the conventionally desired axial deformation (in the thickness direction of the separator discs) is 15% engineering strain across the melt transition. However, the realized deformation depends on the composition of the separator pellet and surrounding cathode and anode pellets (due to electrolyte transport) as well as the stress state within the separator across the melting transition [10]. Modeling the last topic is the subject of this report. Our objective is to describe the macroscopic thermal, phase change, and mechanical behaviors of the separator material so that when this description is combined with electrochemistry and (porous) fluid flow behavior of the molten electrolyte, we can predictively guide and improve molten salt battery design. Historically, Sandia has invested in molten salt battery research, development, and component production to support a variety of weapon systems [20, 2], which has reulted in a broad range of use requirements that involve short, pulsed responses, wherein a battery must deliver power for one minute or less, to much longer responses which involve power delivery on the order of hours [7]. These use cases involve different thermal-mechanical environments on the battery materials. Hence, a model framework is needed to describe the thermal-mechanics of pressed pellet materials, such as the separator. This paper is laid out as follows. In section 2, experiments are presented that detail the complex, thermal-mechanical-phase change behavior of the separator material. These data determine the required behaviors that the model must capture. In section 3, a finite deformation constitutive model is developed, and consequences of objectivity and the first and second laws of thermodynamics are examined. The constitutive model involves generalized creep behavior that is difficult to integrate in time; the time integration algorithm is discussing in section 4. In section 5, the constitutive model is calibrated and then validated against experiments relevant to battery applications in section 6. Alternative boundary conditions and their effects on calibration and validation are examined in section 7. The paper is then concluded in section 8.

Chapter 2

Experiments

The focus of this work is the behavior of the separator by itself. Thus, the effects of electrolyte flow from the separator to the anode and cathode are not considered here. A suite of tests were performed in 2011-2013 to examine the thermal, mechanical, and phase change behaviors of the separator material. The majority of this data is reported in two memos, [6] and [17]. In this work, only a representative selection of those tests is presented in an effort to tell a simpler story.

We begin with a discussion of the separator pellet manufacturing process reproduced from [14]. Briefly, a target weight fraction of eutectic LiCl-KCl and MgO powders are mixed together such that a specified total mass is achieved. The mixture is fuzed above the electrolyte melting temperature for several hours, and then the solid block is ground back into a powder. The powder is then pressed in a cylindrical die to form pellets of a specified dimensions. Based on the initially specified mass of the mixture, this process results in pellets of controlled density and volume fractions of electrolyte, binder, and void space. We examine pellets in this report that are 6 by 1 mm diameter to thickness. Scanning electron micrographs of the separator pellet before and after a thermal cycle are shown in Fig. 2.1.

We consider LiCl-KCl pellets that are manufactured to be composed of 57% electrolyte (LiCl-KCl), 18% binder (MgO), and 25% void fraction (0% relative humidity air). Near 352 C, the electrolyte melting point divides the cold and hot state behaviors of the composite material. Using an ARES 2 Rheometer (TA Instruments), oscillatory shear measurements were taken beginning at room temperature and sweeping across the phase transition at a temperature rate of 5 C / min. Details of these measurements are reported in reference [6]. The storage and loss shear moduli vs. temperature are reported in Fig. 2.2. Note that the loss modulus is always below the storage modulus by at least an order of magnitude, except within the vicinity of the melting transition, which indicates that the composite material behaves as a solid over most of its temperature range. Through the melting transition, however, both moduli are of equal order, signifying that more complex phenomena are at work. The shear storage modulus shows both temperature and deformation dependence both above and below the melting transition.

Ultrasonics measurements at room temperature confirmed the storage shear modulus (under near traction free conditions) at room temperature and through measurements of the bulk modulus, they inferred Poisson's ratio to be 0.03 [18].

Given the large temperature ranges over which the separator operates, thermal expansion may be important in the mechanics of the separator. Since the separator is an aggregate of electrolyte

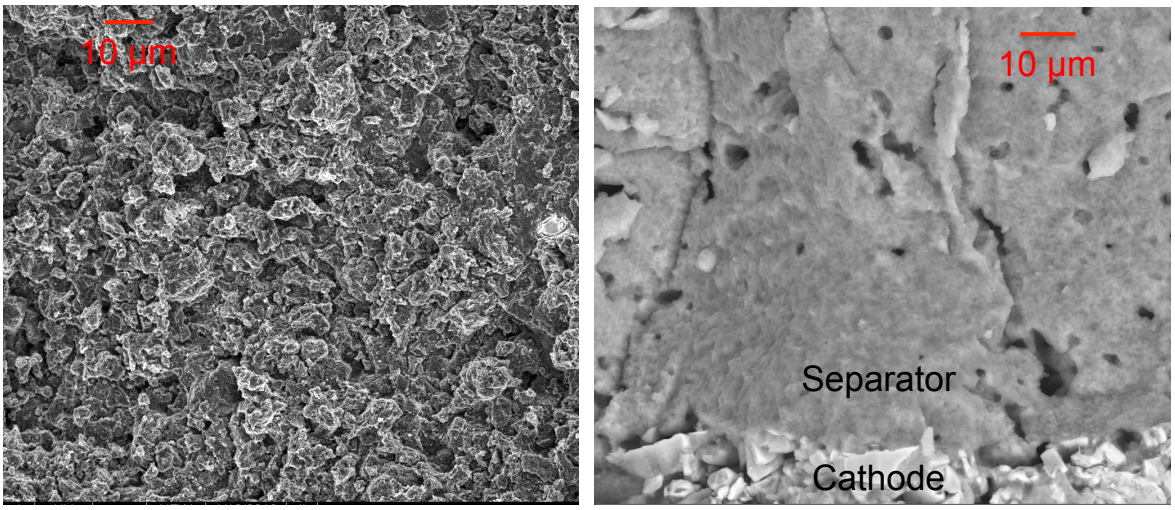

(a) Separator pellet pre-melted microstructure as manufactured

(b) Separator near the cathode interface at room temperature after a thermal cycle under 15 psi applied pressure

Figure 2.1. Scanning electron micrographs of the LiCl-KCl/MgO separator pellet at room temperature as manufactured and after a thermal cycle in which the electrolyte has melted and re-solidified.

and binder particles randomly mixed and pressed together (see Fig. 2.1), we assume thermal expansion to be isotropic and measure it using a NETZSCH dilatometer. In these experiments, a 0.4 psi pressure is applied to the specimen, and the deformation is measured along a single axis during a temperature sweep. An example of this data is presented below for the separator; while hysterisis was expected since the separator compacts as the electrolyte melts, the high temperature expansion coefficient is not consistent between heating and cooling, a result that merits further inquiry. It should be noted that thermal expansion data taken independently on an ARES 2 rheometer conflicts with the pressure dilatometry data, but such measurements are outside the typical usage of the rheometer. In Fig. 2.3, note the difference in linear strain vs. temperature behavior above the transition. That is, immediately after the transition, very little expansion is observed (10E-6 linear strain per C), which is evident from Fig. 2.3, until the temperature direction is reversed, and the specimen is cooled. Still above the melt transition, the thermal expansion behavior is substantially larger (70E-6 linear strain per C). This difference in heating and cooling thermal expansion behavior is not yet understood. However, the expected use case of the model will require the monotonic heating behavior of the material associated with ignition and battery use.

Lastly, we present (also from reference [6]) the height and diameter strain that is observed as a cylindrical separator pellet is heated through the melt transition. This data represents the engineering strain change (per reference diameter and height) between the pre melted and immediately post melted electrolyte states of the separator. The height change is measured across the melt transition, which occurs over a narrow temperature window in which thermal expansion of the instrument,

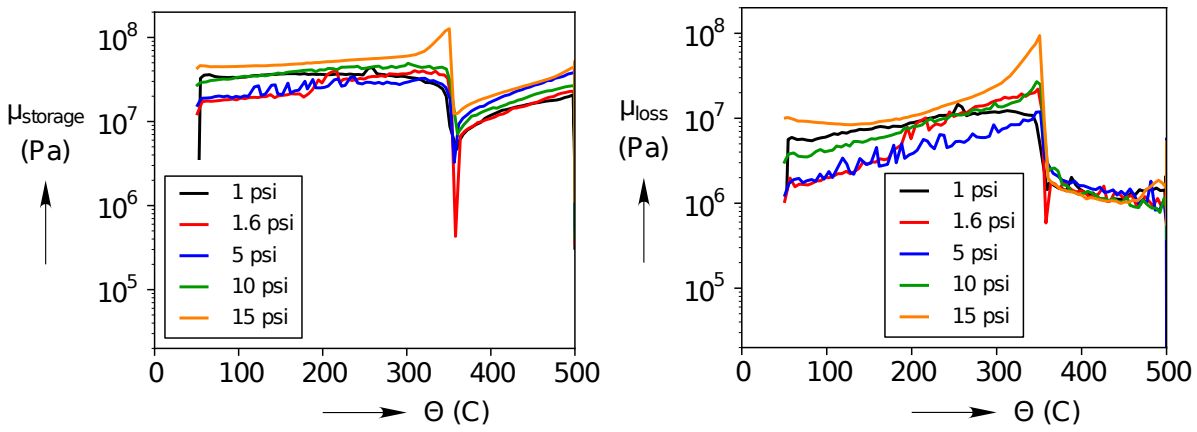

(a) Shear storage modulus vs. temperature

(b) Shear loss modulus vs. temperature

Figure 2.2. Oscillatory shear measurements of 6x1 mm diameter x height separator pellets from room temperature through the melting temperature at 350C are reported under different applied axial stresses. Storage (G') and loss (G") moduli are reported.

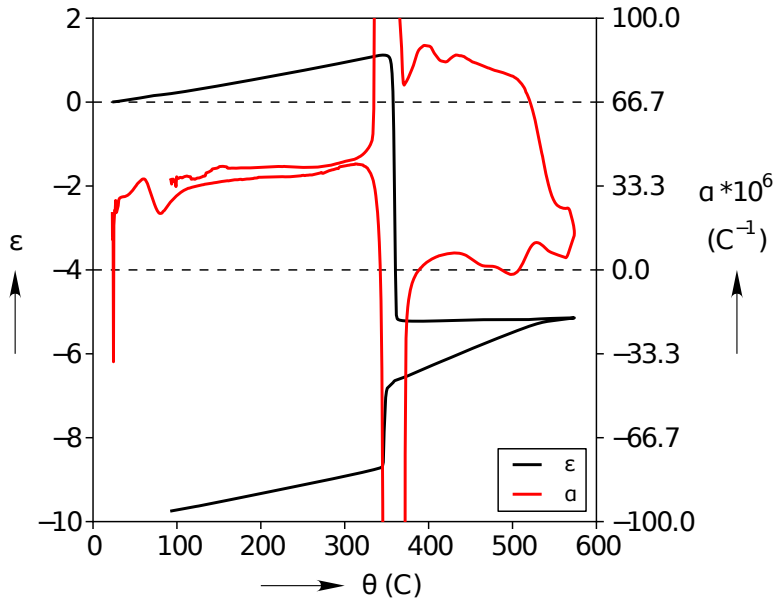

Figure 2.3. Separator pellet linear thermal expansion data taken from pressure dilatometry and a linear LVDT measurement along a single axis.

platen, and specimen are negligible. The diameter strain is an approximate strain measure analyzed from in situ images and measured with the ImageJ software. An image of the specimen at room temperature, a 6x1 mm diameter x height separator pellet, is shown first followed by a plot

of height and diameter engineering strain across the transition that are measured under different states of applied axial stress in Fig. 2.4. These data are consistent with historical data in references [8, 9].

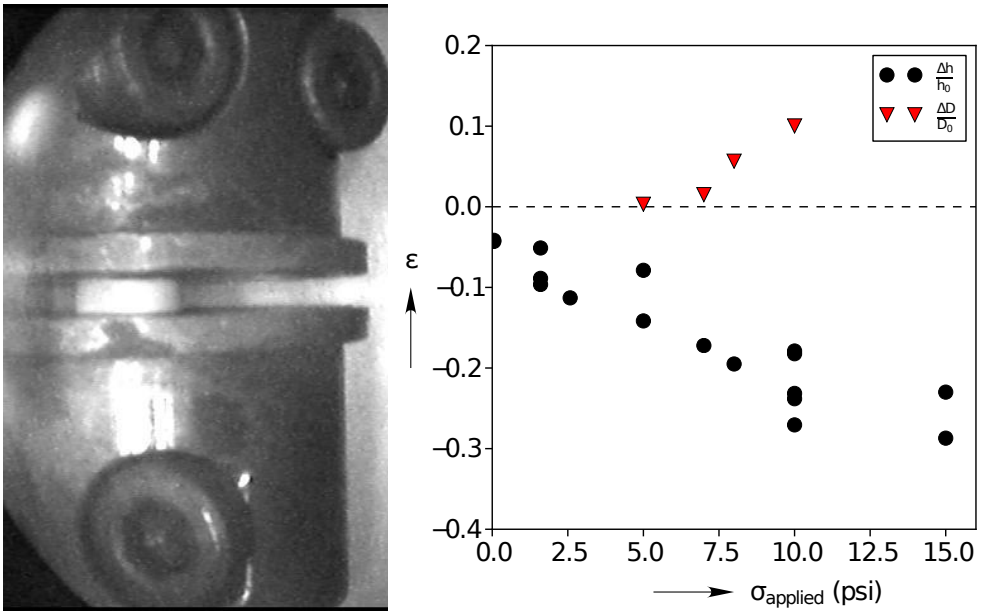

(a) ARES 2 Rheometer Setup Showing a Separator Pellet

(b) Separator Height and Diameter Engineering Strain Across the Melt Transition

Figure 2.4. Separator height and diameter engineering strain across the electrolyte melting transition under different axially applied nominal stresses. The data were measured with an ARES 2 rheometer under a 5C per minute temperature ramp from room temperature through the transition. Diameter strain was measured optically.

A nearly linear relationship between applied axial nominal stress and height strain is observed with an intercept of approximately 4% compressive height strain at zero applied nominal stress. Hence, we conclude that the height change is mechanically driven. That is, the change in shape and volume of the pellet is correlated with the state of stress in the pellet during the electrolyte melting process. Second, because there is a permanent height change even at zero applied stress, capillary forces at the microstructure level are important in determining how the material plastically deforms during this melting process. Finally, although data is lacking near zero applied stress, the height and diameter strain between 5-10 psi axially applied stress indicate a volume change of only a few percent. To see this, the volume strain across the melting transition is given approximately by,

$$\frac{V - V_0}{V_0} = (1 + \varepsilon_h)(1 + \varepsilon_d)^2 - 1. \tag{2.1}$$

Here, V, V_0, ε_h, and ε_d represent the volumes before and after the melt transition and the axial

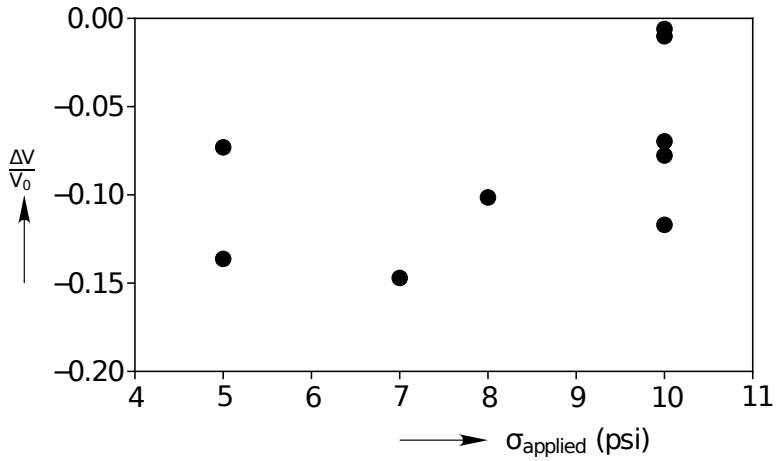

Figure 2.5. Net volume change of the separator pellet as it compacts across the melting transition of the electrolyte under different applied axial stresses from Eq. 2.1 and data in Fig. 2.4.

(height) and diameter engineering strains across the melting transition. From Eq. 2.1, one may plot the volume strain against applied axial stress shown in Fig. 2.5. Note that Eq. 2.1 is an approximation because the cylinder may barrel, but given the relatively large aspect ratio of diameter to height, it is reasonable. Roughly, a 10 % volume change is observed for all the 5-10 psi axial dead loads although substantial scatter in the data renders this statement a conjecture. This volume change arises from the competition between the loss of porosity (diminishing void space) and the expansion of the electrolyte on melting. The specific volume ratio of the melted to solid electrolyte is approximately 20% [14]. Hence, for a separator with 57% by volume electrolyte, 19% MgO binder, and 25% void space in the solid state, a 10% net volume change suggests that the void space is reduces from 25% to 4% (not accounting for thermal and elastic volume changes).

We summarize the main experimental observations necessary for the development of a constitutive model both for the solid skeleton as well as for the combined void, electrolyte, binder material under electrolyte flow free conditions:

- Before and after the electrolyte melts, the separator behaves as a thermo-poro-elastic solid under stresses typically seen within molten salt batteries (order 100 psi). Non-linear behavior is observed for larger stresses and/or large deformation, but this behavior has not been thoroughly characterized and may not be relevant to typical battery applications.

- The separator's shear modulus increases with temperature and applied mean stress

- During the melting of the electrolyte, capillary forces and externally applied stresses cause the void space to diminish. During this process, the separator material deforms significantly as the binder phase reforms a percolated particle network. More deformation is seen with increased applied axial stress.

- Thermal expansion may be important leading up to the electrolyte melting transition if there are significant mismatches between thermal expansion coefficients
- The electrolyte's specific volume change on melting is important during the melting process and competes against the reduction in volume due to the loss of void space

Chapter 3

Model Theory

Modeling separator's complex macroscopic thermal, phase change, and mechanical behaviors are the main challenges of this work. Our objective is to develop a constitutive representation for the fully solid separator in the cold state, the porous solid skeleton (binder phase) in the hot state, and the transition behavior between these two states as the electrolyte melts, which involves significant volume and shape change as seen in Fig. 2.4. This constitutive framework should provide stress contributions to the momentum balance of the solid skeleton, which may be combined with the bulk fluid stress through the effective stress method. Additionally, permanent shape and volume change associated with the evolution of the solid skeleton should be tracked.

Central to simulating the volumetric and shape change associated with the solid skeleton is a physical description of how the binder particles set up a percolated network as the surrounding electrolyte particles melt, wet the binder, and absorb air in the void space. Microscale mechanisms for these processes are not well understood in the materials under examination and remain open scientific questions. A remarkable experimental observation is that the number density of solid, percolated particles supporting structural loads decreases across the electrolyte melt transition as depicted schematically in Fig. 3.1. The schematic does not accurately represent the fractal nature of the binder and electrolyte particles as seen under SEM in Fig. 2.1. It is likely the complexity of the particle geometry that allows such a low binder particle number density to setup a percolated network.

Although the focus of this work is a description of the solid skeleton behavior, here we briefly describe the simulation process flow within the separator as it pertains to species, energy, and momentum balances. At all states of the material, the characteristic length scale of features at the microscale (pore length scale in Fig. 2.1) is typically 2 orders of magnitude smaller than the smallest macroscale dimensions. Hence, we pursue a continuum description of material behavior in which volume fractions of each phase are tracked at material points. In the cold state, the separator behaves as a thermal-elastic solid, and so a Lagrangian description of material points is appropriate *for all phases* represented together with a single set of thermal-mechanical properties. In the hot state, the solid skeleton, which is now a (re-)percolated network of binder particles surrounded by the liquid electrolyte, also behaves as a thermal-elastic and possibly plastic solid. Again, a Lagrangian description of the skeleton is sensible. As is standard practice, the liquid electrolyte (hot state) is represented within an Eulerian frame relative to the (Lagrangian) solid skeleton, and the response of the skeleton and liquid electrolyte are combined through the effective stress method to balance momentum [5]. The combined energy, species, and momentum balance

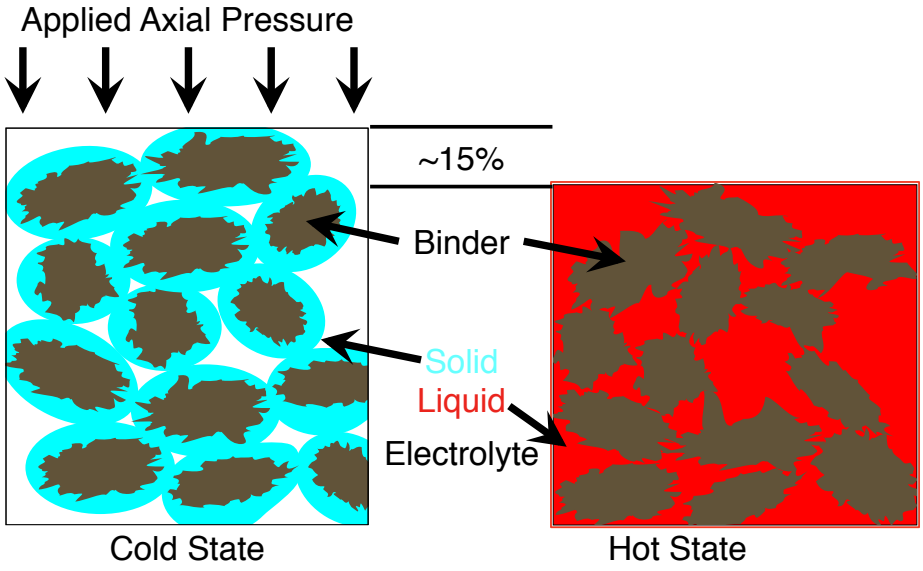

Figure 3.1. Schematic of the separator microstructure in the cold (solid) and hot (saturated porous solid) states. The material compacts by approximately 15% axial strain, the void space disappears (fully saturated state of the fluid), and the binder particles set up a percolated network as depicted here as a network of contact points.

laws are fairly standard in the hot state and very simple, if not trivial, in the cold state.

However, representing the transition between these two states, where the primary deformation of the separator is observed, is more complicated. Here, an extent-of-phase-transition rule of mixtures decomposition of the cold state separator and hot state binder phase is used. Essentially, thermal-elastic properties are interpolated between these two states, and specific creep-based plastic flow rules govern the inelastic deformation of the skeleton during this transition. Models for porous flow through this phase transition have not been finalized as of the writing of this report due to complexities at interfaces between the different layers; we may pursue a fluid viscosity that depends on the extent of electrolyte phase transition.

The separator model described in this section also may be used in a simpler form in which all electrolyte fluid contributions are phenomenologically lumped into the behavior of the solid skeleton, and the loss of porosity, phase change behavior, and inelastic shape change of the separator are phenomenologically considered. Such an approach misses important physics associated with fluid stresses, capillary pressure, and appropriate mechanisms for the loss of porosity (such as dissolution of the gas phase into the molten electrolyte), but this simpler model can be used in a stand alone momentum balance code for quick studies of the separator thermal-mechanical behavior under electrolyte flow-free conditions. They differ in how the Cauchy stress is computed. Either use of the model applies to pressed pellet materials in which a known initial volume fraction of species melts while the other solid species rearranges itself. Therefore, both approaches apply

to the LiCl-KCl-MgO separators and to LiCl-KCl-FeS_2 cathodes. These two model approaches are summarized in Fig. 3.2.

Two Constitutive Model Approaches

	1. Phenomenological	2. Poro-Mechanics
Cold State Solid Thermal-Elastic Behavior	$\sigma = \sigma_{Cold}$	$\sigma = \sigma^{s}_{Cold}$
Electrolyte Melt Transition Cold State+Solid Skeleton +Unsaturated Porous Flow	$\sigma = (1-v_H)\sigma_{Cold} + v_H\sigma_{Hot}$	$\sigma = (1-v_H)\sigma^{s}_{Cold} + v_H\sigma^{s}_{Hot} + Bp^{f}[v_H]\mathbf{1}$
Fully Melted Hot Sate Solid Skeleton+Saturated Porous Flow	$\sigma = \sigma_{Hot}$	$\sigma = \sigma^{s}_{Hot} + Bp^{f}\mathbf{1}$

Figure 3.2. Two approaches to modeling the constitutive behavior of the separator and cathode materials. The phenomenological approach lumps the effects of pressure-saturation into a single phenomenological material that undergoes a phase transition and inelastic deformation. The poro-mechanical approach interpolates between the solid cold state and (partially) saturated hot state with an extent of phase transition viscosity.

As is evident in Fig. 3.2, the Cauchy stress in the phenomenological approach involves an interpolation between responses in the cold and hot states based on a non-dimensional phase transition extent, v_H. Inelastic deformation occurs in the transition region, which will be discussed in subsequent sections, and in the hot state, the material is represented by a single thermal-elastic-plastic response. The poro-mechanical description involves the same thermal-elastic representation in the cold state with a slight notation change to include s, the solid response. As the electrolyte melts, again described with a single progress variable, v_H, the solid skeleton constitutive behavior is again formed through the interpolation between the cold and hot state responses and inelastic deformation, which is applied to both the cold and hot state of the skeleton. In the transition region, a fluid pressure contribution, p^f, also adds to the Cauchy stress and is weighted by the Biot coefficient,

$$B = 1 - \frac{K^f}{K^s}, \tag{3.1}$$

where K^f and K^s are the fluid and solid bulk moduli [5]. The pressure contribution is made to vary with the extent of phase transition to mimic the change in fluid volume as it melts.

At the time in which this report was written, the porous flow capabilities and representation through the melt transition were not complete, such that only the phenomenological approach

was considered. However, these two approaches are similar with respect to the formulation of the solid skeleton and its interpolation between the cold and hot states. Hence, once the porous flow formulation is fully implemented in SIERRA/ARIA, a recalibration and repeat of validation simulations will be required.

The solid skeleton constitutive model is developed inn the sections that follow in the context of the phenomenological approach in Fig. 3.2. We begin by discussing kinematics and assume that we can decompose the deformation gradient multiplicatively into components related to different deformation producing phenomena: thermal expansion and phase transition deformation, change in permanent shape accompanying the melting of the electrolyte, loss of porosity, and mechanical deformation. We discuss the volume fraction decomposition of the macroscale material and how volume fractions are represented on different configurations. Next, we develop a Helmholtz free energy per unit mass to represent the thermal-phase change-loss of porosity-mechanical behavior of the separator material. From this free energy and thermodynamics presented in the appendices, we derive the Cauchy stress, thermodynamic properties, and the equation of motion for the temperature field. We check that our model is objective with respect to Galillean changes of frame. Finally, we look at specific forms for modeling thermal expansion, phase transformation kinetics, and the permanent deformation accumulated due to the loss of porosity as the separator material is initially heated through the melt transition of the electrolyte.

3.1 Kinematics of the Solid Skeleton

Consider a homogenous body, which occupies the volume Ω_0, along with its boundary, $d\Omega_0$. The configuration that it initially occupies is taken to be the time-independent reference configuration. The position of a material point within Ω_0 is denoted by, $\boldsymbol{X} \in \Omega_0$. The motion of a material point from its position, $\boldsymbol{X}$, in the reference configuration to its position, $\boldsymbol{x}$, in the current configuration (with the volume Ω and an associated boundary $\partial\Omega$), is assumed to be a smooth, bijective mapping, so that the inverse mapping always exists. Note, the concept that a macroscale material point tracks a unique cluster of particles at the microscale is questionable during the melt transition of the electrolyte since the binder phase particles rearrange themselves to form a percolated network. Hence, at the microscale, two binder particles initially near each other in the cold state may not be in the hot state, which suggests that the concept of a material point may not be valid at the macroscale. We acknowledge this issue but assume that the traditional Lagrangian perspective of a material point remains a reasonable approach. The material point's motion, displacement field $\boldsymbol{u}$, deformation gradient, and its determinant are,

$$\boldsymbol{x} = \chi(\boldsymbol{X}) = \boldsymbol{X} + \boldsymbol{u}, \qquad \boldsymbol{F} = \frac{\partial \chi(\boldsymbol{X})}{\partial \boldsymbol{X}}, \qquad J = \det(\boldsymbol{F}) > 0. \tag{3.2}$$

We multiplicatively decompose the deformation gradient associated with the cold state combined material and hot state solid skeleton into three components associated with different phenomena:

- $\boldsymbol{F}^{\Theta}$, volumetric deformation due to thermal expansion of each phase, the specific volume

changes associated to melting of the electrolyte, the loss of void (air) space, and transport of the electrolyte phase

- $\boldsymbol{F}^X$, permanent shape and volume change of the solid skeleton during the cold-to-hot phase transition
- $\boldsymbol{F}^M$, elastic deformation experienced by the cold state solid and hot state solid skeleton

Note, the same multiplicative split is used for the solid phase(s) above and below the melt transition. This multiplicative kinematic split is shown in Fig. 3.3 and is described Eq. 3.3.

$$\boldsymbol{F} = \boldsymbol{F}^M \boldsymbol{F}^X \boldsymbol{F}^\Theta = \frac{\partial \boldsymbol{x}}{\partial \boldsymbol{X}}, \tag{3.3}$$

We require that all multiplicative components of the deformation gradient are non-singular since

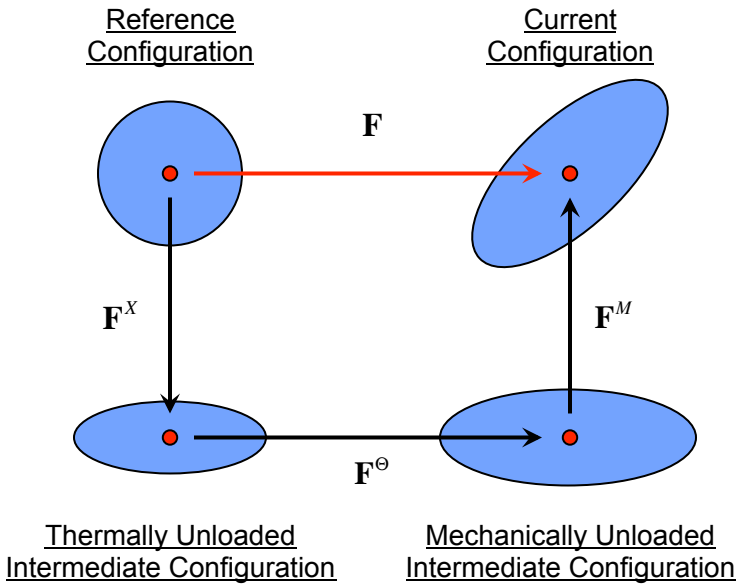

Figure 3.3. Kinematics of a material point (red dot) and its immediate neighborhood. Intermediate configurations are named based on the action of the deformation gradients that connect them. The deformations are exaggerated to distinguish configurations. Note that the reference configuration does not necessarily correspond to a stress-free configuration.

they represent smooth, bijective mappings of material points between configurations, and therefore, we preserve our requirement that the total mapping remains bijective. Consequently,

$$J = J_M J_X J_\Theta, \qquad J_\Theta > 0, J_X > 0, J_M > 0. \tag{3.4}$$

We now further multiplicatively split each of these deformation gradients into volumetric and isochoric components, so that for any one of these components of the deformation gradient, we have,

$$\boldsymbol{F}^{\beta} = \left(J_{\beta}^{\frac{1}{3}}\mathbf{1}\right)\left(J_{\beta}^{-\frac{1}{3}}\boldsymbol{F}^{\beta}\right) = \boldsymbol{F}^{\beta vol}\bar{\boldsymbol{F}}^{\beta}, \qquad \beta = \Theta, X, M. \tag{3.5}$$

Here, $\mathbf{1}$ represents the identity tensor. We define the mechanical Cauchy-Green deformation tensor, which exists on the mechanically unloaded intermediate configuration in Fig. 3.3, and we define the first two invariants of its isochoric part,

$$\boldsymbol{C}^{M} = \boldsymbol{F}^{MT}\boldsymbol{F}^{M} = \boldsymbol{C}^{Mvol}\bar{\boldsymbol{C}}^{M}, \tag{3.6}$$

$$\bar{I}_{1M} = \mathrm{tr}\bar{\boldsymbol{C}}^{M}, \qquad \bar{I}_{2M} = \frac{1}{2}\left((\mathrm{tr}\bar{\boldsymbol{C}}^{M})^{2} - \mathrm{tr}(\bar{\boldsymbol{C}}^{M}\bar{\boldsymbol{C}}^{M})\right). \tag{3.7}$$

3.2 Volume Fraction Decomposition

The volume fraction decomposition of the material into the void, electrolyte, and binder phases plays a significant role in producing volume and shape changes within the material. First consider the decomposition of the macroscale material's specific volume in the current configuration into volumes per unit composite material mass associated with void, electrolyte, and binder constituents and require that the current configuration volume fractions sum to unity,

$$V = V_v + V_e + V_b. \tag{3.8}$$

$$\frac{V_v}{V} + \frac{V_e}{V} + \frac{V_b}{V} = f_v + f_e + f_b = 1 \tag{3.9}$$

Next, using Eq. 3.2, Eq. 3.4, and properties of the deformation gradient, define the ratio of the macroscale composite material's specific volume in the current and reference configurations,

$$\frac{V}{V_0} = J = J_M J_X J_\Theta = \frac{V_v}{V_0} + \frac{V_e}{V_0} + \frac{V_b}{V_0} = f_v^0 + f_e^0 + f_b^0. \tag{3.10}$$

Clearly, $Jf_i = f_i^0$ for i as e, v, and b. In general, properties such as thermal expansion and the bulk modulus of the three phases will differ. Consequently, the volume changes experienced by different phases will not be experienced equally, and in the coupled poro-mechanical approach, such differences in bulk moduli and volumetric deformation are accounted for through the Biot coefficient in Eq. 3.1, and tracking of these volume fractions at material point is not needed. For the phenomenological approach in which all constituents are lumped together, we expect that the loss of porosity (gas phase) and specific volume change of the electrolyte on melting will dominate the volume change behavior of the separator material since both of these behaviors are significantly

larger than thermal expansion and elastic volume changes of the solid skeleton. Solving for the volume ratio associated with macroscopic thermal expansion and phase volume changes,

$$J_\Theta = J_M^{-1} J_X^{-1} \left(f_v^0 + f_e^0 + f_b^0 \right) = f_v^\Theta + f_e^\Theta + f_b^\Theta, \tag{3.11}$$

wherein these last volume fractions exist within an elastically and plastically unloaded configuration (from the solid skeleton) and define the volume deformation, J_Θ, due to changes in volume fraction and or phase decomposition of each constituent. With a bit of algebra, these volume fractions are related to the current configuration volume fractions in Eq. 3.9 via,

$$f_v^\Theta = f_v J_\Theta, \qquad f_e^\Theta = f_e J_\Theta, \qquad f_b^\Theta = f_b J_\Theta, \tag{3.12}$$

which are known from porous-flow calculations and the thermodynamic state of each constituent. Note that eqs. 3.11 and 3.12 are approximations that assume that each constitutent phase experiences the same volume change associated with the skeletons elastic and plastic volumetric motions and may not be reasonable.

3.3 Helmholtz Free Energy Density and Work-Conjugate Thermodynamic Fluxes

We derive the thermal mechanical behavior of the separator from a specific Helmholtz free energy following appendices A and B. Ignoring chemical changes in the separator material, we assume that the specific Helmholtz free energy density is composed of elastic and thermal contributions, which we model with a volume fraction weighted sum of the associated cold state aggregate material and hot state binder phase solid skeleton in Eq. 3.14. Note that "C" and "H" denote the cold and hot states properties respectively; however, fundamentally, these two states are different (ie. the cold state is the binder + solid electrolyte while the hot state is a the re-percolated binder phase).

$$\begin{aligned} \rho_0 \psi \left(\Theta, \boldsymbol{C}^M \right) = \\ v_C \left(\frac{\kappa_C[\Theta]}{2} \left(J_M^2 - 1 - 2\log[J_M] \right) + \mu_C[J_M, \Theta] \left(\bar{I}_{1M} - 3 \right) \right) \dots \\ + v_H \left(\frac{\kappa_H[\Theta]}{2} \left(J_M^2 - 1 - 2\log[J_M] \right) + \mu_H[J_M, \Theta] \left(\bar{I}_{1M} - 3 \right) \right) \dots \\ + \rho_0 \left(v_C C_{VC} + v_H C_{VH} \right) \left(\frac{\Theta^2 - \Theta_{MELT}^2}{2\Theta_{MELT}} \right) \end{aligned} \tag{3.13}$$

Here, μ_C (μ_H) and κ_C (κ_H) are the temperature and mechanical deformation dependent shear and bulk moduli of the cold (hot) state respectively while the specific heat capacities at constant states

of mechanical deformation are denoted by C_{VC} and C_{VH}. These material properties correspond the composite material's response above and below the meling transition of the electrolyte, Θ_{MELT}. We have used a Neo-Hookean constitutive model for the elastic free energies of the cold and hot states with $\bar{I}_{1M}$ denoting the first invariant of the isochoric Cauchy-Green deformation tensore (Eq. 3.7).

We now calculate the Cauchy stress and entropy density using Eq. 3.14 and the Rational mechanics approach. Following Eq. B.8, we calculate the Second-Piola Kirchoff-like stress tensor defined on the mechanically unloaded configuration, and then push it forward to arrive at the Cauchy stress,

$$\begin{aligned} \boldsymbol{S}^M = 2\frac{\partial \Psi}{\partial \boldsymbol{C}^M} = \dots \\ \left(v_C \mu_C[J_M,\Theta] + v_H \mu_H[J_M,\Theta]\right) J_M^{-\frac{2}{3}} \left(\mathbf{1} - \frac{\mathrm{tr}\boldsymbol{C}^M}{3}\boldsymbol{C}^{M-1}\right) + \dots \\ \dots \left(v_C \frac{\partial \mu_C}{\partial J_M} + v_H \frac{\partial \mu_H}{\partial J_M}\right)(\bar{I}_{1M} - 3) J_M \boldsymbol{C}^{M-1} + \dots \\ \dots \left(v_C \kappa_C[\Theta] + v_H \kappa_H[\Theta]\right)\left(J_M^2 - 1\right)\boldsymbol{C}^{M-1}, \end{aligned} \tag{3.14}$$

$$\begin{aligned} \sigma_{ij} = 2J_M^{-1}\boldsymbol{F}^M \frac{\partial \psi}{\partial C_{pk}^M}(\boldsymbol{F}^M)^T = \dots \\ \left(v_C \mu_C[J_M,\Theta] + v_H \mu_H[J_M,\Theta]\right) J_M^{-\frac{5}{3}} \left(\boldsymbol{F}^M(\boldsymbol{F}^M)^T - \mathbf{1}\right) + \dots \\ \dots \left(v_C \frac{\partial \mu_C}{\partial J_M} + v_H \frac{\partial \mu_H}{\partial J_M}\right)(\bar{I}_{1M} - 3)\mathbf{1} + \dots \\ \dots \left(v_C \kappa_C[\Theta] + v_H \kappa_H[\Theta]\right)\left(J_M - J_M^{-1}\right)\mathbf{1}. \end{aligned} \tag{3.15}$$

and the referential entropy density (from Eq. B.8) is,

$$\begin{aligned} \eta_0 = -\left(v_C \frac{d\kappa_C}{d\Theta} + v_H \frac{d\kappa_H}{d\Theta}\right)\left(J_M^2 - 1 - 2\log[J_M]\right) \dots \\ \dots - \left(v_C \frac{\partial \mu_C}{\partial \Theta} + v_H \frac{\partial \mu_H}{\partial \Theta}\right)(\bar{I}_{1M} - 3) \dots \\ \dots - \rho_0 \left(v_C C_{VC} + v_H C_{VH}\right)\left(\frac{\Theta}{\Theta_{MELT}}\right). \end{aligned} \tag{3.16}$$

3.4 Thermal and Phase Change Properties

We define the heat capacity per unit current volume of the material at a constant state of mechanical deformation and relate it to the Helmholtz free energy density in Eq. 3.14 through the Legendre

transform, Eq. B.4, and the relationship between it and the entropy density, Eq. B.8,

$$C_V = J\rho_0 \left(\frac{\partial \varepsilon_0}{\partial \Theta} \right) = -\Theta J \rho_0 \left(\frac{\partial^2 \Psi}{\partial \Theta \partial \Theta} \right) = \dots \tag{3.17}$$
$$-\Theta J \left(v_C \frac{d^2 \kappa_C}{d\Theta^2} + v_H \frac{d^2 \kappa_H}{d\Theta^2} \right) \left(J_M^2 - 1 - 2\log[J_M] \right) \dots$$
$$\dots - \Theta J \left(v_C \frac{\partial^2 \mu_C}{\partial \Theta^2} + v_H \frac{\partial^2 \mu_H}{\partial \Theta^2} \right) (\bar{I}_{1M} - 3)$$
$$\dots - J\rho_0 \left(v_C C_{VC} + v_H C_{VH} \right) \left(\frac{\Theta}{\Theta_{MELT}} \right).$$

Note that the composite density in the reference configuration, ρ_0, is not a constant since the void volume fraction diminishes and the electrolyte expands during its phase change. Also note that in the absence of curvature of the shear and bulk moduli with temperature, the heat capacity is given by a rule of mixtures between the hot and cold states of the composite material.

To arrive at the equation of motion for the temperature field, we use Eq. B.8, the material time derivative of the Helmholtz free energy, Eq. B.6, the energy balance, Eq. A.5, the heat capacity per unit volume, Eq. 3.17, and the mechanical Cauchy-Green deformation tensor, Eq. 3.6, to arrive at,

$$C_V \dot{\Theta} = Q - \boldsymbol{\nabla}_X \bullet \boldsymbol{Q} \tag{3.18}$$
$$\dots + \Theta \frac{\partial^2 \Psi}{\partial \Theta \partial \boldsymbol{C}^M} : \dot{\boldsymbol{C}}^M + \sum_\beta \left(\Theta \frac{\partial^2 \Psi}{\partial \Theta \partial Z^\beta} - \frac{\partial \Psi}{\partial Z^\beta} \right) \dot{Z}^\beta.$$

We now consider the thermostatics associated with the electrolyte's solid to liquid phase transition. There are at least two choices to model this phenomenon. The simpler approach is to approximate the latent heat capacity of the composite material as the difference of the macroscopically measured heat capacities between the hot (electrolyte melted) and cold (electrolyte solid) states. That is,

$$\rho_0 L_{trans} = \Theta_{MELT} \left(C_{CF_M} - C_{HF_M} \right), \tag{3.19}$$

which is correct provided there is no mass transport. Although these are heat capacities at a fixed state of deformation, see Eq. 3.17, they do account for stored elastic strain energy in the system. Eq. 3.19, essentially represents the difference in thermal energy stored in the two states of the composite material. The second approach considers the change in heat capacities of the individual components and combines them in a volume fraction weighted rule of mixtures. That is, the change in heat capacity of the electrolyte, MgO, and air in the void space as well as mass transfer into and out of the material point. For now, the first approach is used as it is simpler to measure with standard macroscale tests.

In addition to a jump in the stored thermal energy, melting the electrolyte changes the specific volume of that phase and hence of the composite material. The jump in specific volume of the electrolyte, $\gamma = \frac{V_{melt}}{V_{solid}}$, is a material property that depends on the specific composition. Since typically a eutectic composition of KCl and LiCl is used, we assume that the specific volume change corresponds to that measured at the eutectic composition, and so we do not consider the effects of deviations about this eutectic composition. Thus, the specific volume of the electrolyte has the following form

$$V_e = V_{e0}\left(v_H\gamma + v_C(1)\right) = V_{e0}\left(1 + v_H(\gamma - 1)\right), \tag{3.20}$$

wherein V_{e0} is the electrolyte's specific volume in the solid phase that has been unloaded by the elastic and plastic volume changes of the skeleton. Returning to Eq. 3.11, as the electrolyte melts, the composite material changes volume as,

$$J_X = f_v^X + f_e^X\left(1 + v_H(\gamma - 1)\right) + f_b^X. \tag{3.21}$$

Implicit in Eq. 3.21 is the assumption that the change is volume to the electrolyte phase change is isotropic, which is reasonable since we are representing an aggregate number of randomly oriented particles.

Next, we model the (isotropic) thermal expansion of the composite material in the cold and hot states,

$$\begin{aligned} \boldsymbol{F}^{\Theta} &= J_{\Theta}^{\frac{1}{3}}\mathbf{1}, \\ \text{if} \quad \Theta < \Theta_{MELT}, &\quad J_\Theta = \exp\left[\alpha_C(\Theta - \Theta_0)\right], \\ \text{elseif} \quad \Theta \geq \Theta_{MELT} &\quad J_\Theta = \exp\left[\alpha_C(\Theta_{MELT} - \Theta_0) + \alpha_H(\Theta - \Theta_{MELT})\right]. \end{aligned} \tag{3.22}$$

Here, α_C and α_H are the (constant) linear thermal expansion coefficients of the cold and hot states respectively. Although in reality the different phases will have different thermal expansion behaviors, the composite rule of mixtures approach allows for simple macroscale measurements and calibration, and so again, we pursue the simpler approach.

3.5 Electrolyte Phase Transformation Kinetics

We model the melting/solidification kinetics of the electrolyte through one of two approaches. The simpler approach requires the melting temperature, Θ_{MELT} and phase transition temperature width, Θ_{MW} as input parameters. A linear interpolation is then executed between the cold and hot states of the composite material, which is assumed to coincide with the solid and liquid phase decomposition of the electrolyte. Hence, under this approach, the volume fractions of cold and hot

state material are,

$$\begin{aligned} &\text{if} \quad \Theta < \Theta_{MELT} - \frac{\Theta_{MW}}{2}, \quad v_H = 0, \\ \text{elseif} \quad 2|\Theta - \Theta_{MELT}| \leq \Theta_{MW}, \quad &v_H = \frac{\Theta - \Theta_{MELT} + \Theta_{MW}/2}{\Theta_{MW}}, \\ &\text{else} \quad v_H = 1. \end{aligned} \tag{3.23}$$

We require always that the total volume fraction of cold and hot states sum to unity,

$$v_C + v_H = 1. \tag{3.24}$$

The second model description of the electrolyte phase transition represents the process with thermally activated (Arrhenius) kinetics. That is, the melting transition is treated as if it is a reversible chemical reaction between the cold and hot states ($C \leftrightarrow H$). The rate at which the volume fraction of the cold state changes is modeled as,

$$\frac{dv_C}{dt} = -k_{AB} v_C + k_{BA} v_H. \tag{3.25}$$

The volume fractions obey the conservation statement in Eq. 3.24, and at equilibrium, the volume fractions from Eq. 3.25 relate the forward and reverse transition rates to a temperature dependent equilibrium constant,

$$\frac{v_{Beq}}{v_{Aeq}} = \frac{k_{AB}}{k_{BA}} = K_{EQ}[\Theta] = \exp\left\{ -\frac{h_{xform}}{R\Theta} + \frac{\eta_{xform}}{R} \right\}. \tag{3.26}$$

The transition temperature, Θ_{MELT}, is defined by ratio of the enthalpy and entropy of the transition,

$$\Theta_{MELT} = \frac{h_{xform}}{\eta_{xform}} \tag{3.27}$$

The forward and reverse transition rates are represented through an Arrhenius relationship and consideration of Eq. 3.26,

$$k_{AB} = k_0 \exp\left\{ -\frac{E_{ACT}}{R\Theta} \right\}, \tag{3.28}$$

$$k_{BA} = \frac{k_{AB}[\Theta]}{K_{EQ}[\Theta]}. \tag{3.29}$$

Here, R is the universal gas constant. With this approach, the two required material parameters, h_{xform}, η_{xform} determine the melting temperature and transition width. Additionally, the thermal activation energy, E_{ACT}, and the temperature dependent equilibrium constant, $K_{EQ}(\Theta)$, are required input parameters, and these allow for some flexibility in super cooling/heating the unstable phase.

One weakness of this approach to modeling the phase transition kinetics as a thermally-activated process is that it cannot account for the fact that a phase transition can be driven by mechanical work (in accordance with the energy balance equations A.5 or 3.18) or changes to internal variables. For the molten salt battery considered here, the phase transition is driven by thermal energy, and so this model of phase change kinetics as a reversibly reacting system implicitly requires a specific heat flux Q_i or volumetric heating rate Q to occur such that the energy balance is satisfied (Eq. 3.18).

Finally, it is also possible for the model to take the phase decomposition as an input directly from the energy balance. This approach relies on an external representation of the thermodynamic state of the composite material.

3.6 Loss of Void Space

During the melting of the electrolyte, the microstructure of the separator irreversibly changes, and macroscopically both volumetric and isochoric motions are observed. Volumetric deformation is associated with the loss of void volume fraction as trapped gas within the material either escapes or dissolves into the liquid electrolyte. This reduction in volume is opposed by the specific volume increase of the electrolyte across its melt transition [14]. The mechanism by which the void volume fraction evolves is not fully understood. Additionally, the liquid electrolyte wets the MgO binder, which generates capillary forces that further compress the composite material and/or contribute to the loss of void space [16, 14, 8, 10]. Under full poro-mechanical coupling, the loss of void space (inversely related to the rise in saturation) is directly computed. For the electrolyte flow-free conditions considered here, we phenomenologically model this loss of void space as a mean stress driven process. Specifically, if porous flow is not considered, then the loss of void volume fraction, as defined in Eq. 3.11 and 3.12, via the following rule,

$$\dot{f}_v^X = C_1 \dot{v}_H f_v^X \left(J_M - 1\right)^p \operatorname{sign}\left(J_M - 1\right)^{p-1} \tag{3.30}$$

Here, C_1 is a phenomenological material constant that associates the loss of void space, which is tied to volumetric deformation through Eq. 3.11, and elastic volumetric deformation through $J_M - 1$. The exponent, p, is a positive integer greater than or equal to zero. Thus, when the composite material is subjected to a compressive state of stress, $J_M - 1 < 0$, and and so the void fraction diminishes. Concomitantly, J_X also diminishes through Eq. 3.11. If the composite material were to be subjected to a tensile environment, $J_M - 1 > 0$, and the void fraction would grow. This latter case is not anticipated to occur in thermal batteries. This form of the evolution rule is thermodynamically consistent with respect to the second law, Eq. B.9 whereas such compliance is

not guaranteed if the void volume fraction is required to diminish while the material point is under both tensile and compressive hydrostatic stress. Hence, to enforce thermodynamic consistency, we add the factor, $\text{sign}\,(J_M - 1)^{p-1}$.

We now return to Eqs. 3.11 and 3.21, which characterize the volume change due to the electrolyte expansion and loss of void space. Provided that there is no transport of the binder, then f_b^X is a constant. Then, J_X is determined from the evolution of f_v^X in Eq. 3.30 and from f_b^X at the initial state of the material provided the evolution of f_e^v is known. In the absence of porous flow modeling, we will assume the mass of electrolyte per unit reference volume of the composite material is fixed, which implies that there is no net transport of the electrolyte into a material volume. Alternatively, when porous flow calculations are considered, then the electrolyte concentration (and hence volume fraction) is an input variable to the constitutive model. In either case, the effects on the mechanically and thermally unloaded volume are captured through J_X.

3.7 Isochoric Plasticity During the Melt Transition

The liquified separator no longer supports structural loads, and so shear stresses are transferred to the MgO binder skeleton. However, as depicted in Fig. 3.1, we conjecture that the binder particles undergo significant rearrangement to set up a load bearing, percolated network. We associate the observed shape change in melting separator pellets with this process, and we assume the binder particle rearrangement to correspond to an isochoric motion at the macroscale. Data in Fig. 2.4(b) suggests that the shape change is at a basic level stress-driven. We anticipate that the key to representing the macroscale isochoric inelastic response is to adequately represent how the binder particles setup a percolate network at the microscale. Without this underlying mechanism well understood, we proceed with a phenomenological generalized creep model to represent the macroscale isochoric inelastic deformation of the separator material and solid skeleton under flow free and porous flow conditions respectively. The rate of isochoric plastic deformation is defined on the mechanically unloaded configuration (see Fig. 3.3) is tied to the loss of void space volume fraction through,

$$\overline{\boldsymbol{D}}^X = \frac{C_2|\dot{f}_v^X|}{\mu}\boldsymbol{C}^M\boldsymbol{S}_{dev}^M\boldsymbol{C}^M, \tag{3.31}$$

which is related to the isochoric inelastic velocity gradient on the same configuration through,

$$\dot{\overline{\boldsymbol{F}}}^X\overline{\boldsymbol{F}}^{X-1} = \overline{\boldsymbol{L}}^X = \boldsymbol{C}^{M-1}\overline{\boldsymbol{D}}^X = \frac{C_2|\dot{f}_v^X|}{\mu}\boldsymbol{S}_{dev}^M\boldsymbol{C}^M. \tag{3.32}$$

In these equations, C_2 represents a phenomenological material constant that scales the rate of isochoric inelastic flow with the deviatoric stress state (defined on the intermediate configuration) and rate at which the void fraction is diminishing. The deviatoric mechanical Second Piola-Kirchoff

stress is defined through the following relationship,

$$\boldsymbol{S}^{M}_{dev} = \boldsymbol{S}^{M} - \frac{1}{3}\left(\boldsymbol{S}^{M} : \boldsymbol{C}^{M}\right)\boldsymbol{C}^{M-1} = \ldots \tag{3.33}$$
$$\left(v_C \mu_C[J_M,\Theta] + v_H \mu_H[J_M,\Theta]\right) J_M^{-\frac{2}{3}} \left(\mathbf{1} - \frac{\mathrm{tr}\boldsymbol{C}^{M}}{3}\boldsymbol{C}^{M-1}\right)$$

following from Eq. 3.14, which is different from the traditional definition of a deviatoric tensor on the current configuration. This difference arises because the metric tensor is $\boldsymbol{C}^{M-1}$ on the mechanically unloaded configuration (see Fig. 3.3) rather than $\mathbf{1}^{-1} = \mathbf{1}$ on the current configuration. The formalism in this section follows references [22, 1] with one important difference; here, isochoric plastic flow is driven by the loss of porosity (diminishing f_v^X) and involves no yield surface.

Note, the isochoric plastic velocity gradient, Eq. 3.32 along with the deviatoric part of the mechanical Second Piola-Kirchoff stress, Eq. 3.33, furnishes the evolution rule for the isochoric plastic flow portion of $\overline{\boldsymbol{F}}^{X}$. This rule is phenomenological and can be replaced or improved as new experimental data is obtained that better informs us of what mechanisms drive the permanent shape change of the MgO binder as the electrolyte melts.

3.8 Shear and Bulk Moduli Dependencies

Evident from the dynamic mechanical analysis data, the storage and loss shear moduli are both temperature and deformation dependent in both the cold and the hot states. Furthermore, the sensitivity to deformation and temperature appears to be higher in the cold state than in the hot state, so that distinct dependencies in the two states are required. We assume that the deformation dependence of the moduli arises from volumetric mechanical deformation, $J_M - 1$. Thus, the equilibrium shear and bulk moduli in the cold and hot states are assumed to obey the following forms,

$$\kappa_\beta(\Theta) = \kappa_{\beta 0} + \kappa_{\beta 1}\left(\Theta - \Theta_{MELT}\right) \tag{3.34}$$
$$\mu_\beta(\Theta) = \mu_{\beta 0} + \mu_{\beta 1}\left(\Theta - \Theta_{MELT}\right) + \mu_{\beta 2}\left(J_M - 1\right)\ldots \tag{3.35}$$
$$+\mu_{\beta 3}\left(\Theta - \Theta_{MELT}\right)\left(J_M - 1\right)$$

Here, β represents either the cold state (C) or the hot state (H). Note that the bulk moduli are assumed not to be deformation dependent following experimental observations. The entities $\kappa_{i\beta}$ and $\mu_{i\beta}$ represent six material constants for each phase.

Aside, rheometry measurements show loss moduli substantially lower than the storage moduli especially well away from the transition, which is consistent with our interpretation that the composite material behaves as a solid even as one of its constituent materials melts. We do not consider (viscoelastic) loss mechanisms to represent the loss moduli observed except for the plastic

flow behavior already discussed, which is only active within the vicinity of the electrolyte phase transition.

3.9 Objectivity Requirements

We must ensure that the constitutive response is independent of the frame in which we choose to observe our system. Following standard procedures in the literature, see references [11, 22], we introduce an arbitrary and time-dependent change of frame by applying a rigid-body rotation, $\boldsymbol{R}(t)$ and translation $\boldsymbol{c}(t)$ of the body in the current configuration. The spatial position, $\boldsymbol{x}$, of a material point is mapped to $\boldsymbol{x}^*$, and consequently, the deformation gradient is also transformed to $\boldsymbol{F}^*$ following,

$$\boldsymbol{x}^* = \boldsymbol{R}\boldsymbol{x} + \boldsymbol{c}, \qquad \boldsymbol{F}^* = \frac{\partial \boldsymbol{x}^*}{\partial \boldsymbol{X}} = \boldsymbol{R}\boldsymbol{F}. \tag{3.36}$$

Since the reference configuration is fixed in time, it is unaffected by this transformation. Scalars, also, are invariant to a change in frame (since $\boldsymbol{R}$ is an orthogonal transformation). However, the Helmholtz free energy, and consequently the Cauchy stress (after the push forward with $\boldsymbol{F}^M$) depend on the left mechanical Cauchy-Green tensor ($\boldsymbol{C}^M$, which we show here to be frame invariant. Using Eqs. 3.36 and 3.3, we show

$$\begin{aligned} \boldsymbol{C}^{M*} &= (\boldsymbol{F}^{M*})^T \boldsymbol{F}^{M*} = (\boldsymbol{F}^X)^{-T} (\boldsymbol{F}^\Theta)^{-T} \boldsymbol{F}^T \boldsymbol{R}^T \boldsymbol{R} \boldsymbol{F} (\boldsymbol{F}^\Theta)^{-1} (\boldsymbol{F}^X)^{-1} \dots \\ &\dots = (\boldsymbol{F}^X)^{-T} (\boldsymbol{F}^\Theta)^{-T} \boldsymbol{F}^T \boldsymbol{F} \boldsymbol{F}^\Theta)^{-1} (\boldsymbol{F}^X)^{-1} = (\boldsymbol{F}^M)^T \boldsymbol{F}^M = \boldsymbol{C}^M \end{aligned} \tag{3.37}$$

Lastly, we ensure that the Cauchy stress is frame indifferent,

$$\begin{aligned} \boldsymbol{F}^{M*} &= \boldsymbol{R}\boldsymbol{F}^M = \boldsymbol{R}\boldsymbol{F}(\boldsymbol{F}^\Theta)^{-1}(\boldsymbol{F}^X)^{-1}, \\ \boldsymbol{\sigma}^* &= 2J_M^{-1} \boldsymbol{F}^{M*} \frac{\partial \psi}{\partial \boldsymbol{C}^{M*}} (\boldsymbol{F}^{M*})^T = \boldsymbol{R} \left(2J_M^{-1} \boldsymbol{F}^M \frac{\partial \psi}{\partial \boldsymbol{C}^M} \boldsymbol{F}^M \right) \boldsymbol{R}^T = \boldsymbol{R}\boldsymbol{\sigma}\boldsymbol{R}^T. \end{aligned} \tag{3.38}$$

This latter results conforms to the standard requirements of frame-indifferent second-rank tensors, which demonstrates that the material model is objective. Similar exercises will show that other quantities that appear in the balance laws, such as the referential heat flux ($\boldsymbol{Q}$) also satisfy objectivity requirements.

3.10 Thermal Transport

Although the referential thermal energy flux $\boldsymbol{Q}$ and source Q terms have been employed in the balance law manipulations, typically these quantities are measured and/or constitutively modeled

with respect to quantities in the current configuration. We consider isotropic thermal transport following Fick's second law with a constant diffusivity, D_{TH}, so that the heat flux and heat sources are modeled as,

$$\boldsymbol{q} = -D_{TH}\boldsymbol{\nabla}\Theta, \qquad \boldsymbol{Q} = \boldsymbol{F}^{-1}\boldsymbol{q}, \qquad Q = J^{-1}q. \tag{3.39}$$

3.11 Model Summary

The model described in this document up to 28 parameters depending on the users' choices. These parameters are presented in the following tables. It is important to note that many parameters are optional. For a stand alone momentum balance without considering electrolyte transport and with a prescribed temperature field, then the minimum required parameters are listed in table 3.11. Optional parameters allow for temperature and volumetric deformation dependent elastic moduli, an alternative representation of the phase transition kinetics, as well as thermal properties of the hot and cold state necessary in coupled thermal-mechanical analyses. These parameters are summarized in 3.11. Finally, a summary of the equations that govern the model's thermal and mechanical behavior is given in 3.11.

Parameter	Unit	Description
Θ_{MELT}	K	Melting temperature of the electrolyte
Θ_{MW}	K	Temperature width of the phase transition about Θ_{MELT}
Θ_{C0}	K	Reference temperature of the cold state
Θ_{H0}	K	Reference temperature of the hot state
$\Theta_{\alpha 0}$	K	Temperature datum for thermal expansion
α_C	K^{-1}	Linear thermal expansion coefficient of the cold phase
α_H	K^{-1}	Linear thermal expansion coefficient of the hot phase
γ	none	Ratio of the liquid to solid electrolyte specific volumes
κ_{C0}	Pa	Bulk modulus of the cold state
μ_{C0}	Pa	Shear modulus of the cold state
κ_{H0}	Pa	Bulk modulus of the hot state
μ_{H0}	Pa	Shear modulus of the hot state
f_{v0}	none	Initial volume fraction of voids
f_{s0}	none	Initial volume fraction of the electrolyte
f_{MgO0}	none	Initial volume fraction of the binder
p	none	Exponent that controls the dependence of the void volume fraction evolution on mechanical volume strain
C_1	none	Constant associated with the rate of change of the void volume fraction, f_v^X
C_2	none	Constant Associated with the rate of isochoric plastic deformation, $\overline{\boldsymbol{D}}^X$

Table 3.1. Minimum required parameters for a stand-alone momentum balance analysis or a coupled momentum and energy balance analysis

Parameter	Unit	Description
h_{xform}	J mol^{-1}	Change in enthalpy across the phase transition. Note, this parameter and the subsequent three are used only if (Θ_{MELT}, Θ_{MW}) are not used
η_{xform}	J mol^{-1} K^{-1}	Change in entropy across the phase transition
k_0	none	Pre-factor to the Arrhenius transformation kinetics
E_{ACT}	J mol^{-1}	Activation energy of the Arrhenius transformation kinetics
μ_{C1}	Pa K^{-1}	Linear temperature dependence of the cold state shear modulus
μ_{C2}	Pa	Linear dependence of the cold state shear modulus on mechanical volume strain ($J_M - 1$)
μ_{C3}	Pa K^{-1}	Bi-linear temperature dependence of the cold state shear modulus on temperature and mechanical volume strain
κ_{C1}	Pa K^{-1}	Linear temperature dependence of the cold state bulk modulus
μ_{H1}	Pa K^{-1}	Linear temperature dependence of the hot state shear modulus
μ_{H2}	Pa	Linear dependence of the hot state shear modulus on mechanical volume strain ($J_M - 1$)
μ_{H3}	Pa K^{-1}	Bi-linear temperature dependence of the hot state shear modulus on temperature and mechanical volume strain
κ_{H1}	Pa K^{-1}	Linear temperature dependence of the hot state bulk modulus
C_{VC}	J m^{-3}	Constant specific heat capacity of the cold state for a fixed state of mechanical deformation
C_{VH}	J m^{-3}	Constant specific heat capacity of the hot state for a fixed state of mechanical deformation
D_{TH}	$m^2 s$	Constant thermal diffusivity
ρ_0	kg m^{-3}	Initial (as manufactured) density

Table 3.2. Optional Parameters

Keywords	Equations
Kinematics	$\boldsymbol{F} = \boldsymbol{F}^M \boldsymbol{F}^X \boldsymbol{F}^\Theta = \frac{\partial \boldsymbol{x}}{\partial \boldsymbol{X}}\,, \qquad J = J_M J_X J_\Theta$
Thermal Expansion	$\boldsymbol{F}^\Theta = J_\Theta^{\frac{1}{3}} \mathbf{1},$ if $\quad \Theta < \Theta_{MELT}, \qquad J_\Theta = \exp\left[\alpha_C(\Theta - \Theta_0)\right]$ else $\quad J_\Theta = \exp\left[\alpha_C(\Theta_{MELT} - \Theta_0) + \alpha_H(\Theta - \Theta_{MELT})\right]$
Volume Fractions Per Reference Volume	$J_X = \frac{V_v J_M^{-1} J_\Theta^{-1}}{V_0} + \frac{V_e J_M^{-1} J_\Theta^{-1}}{V_0} + \frac{V_b J_M^{-1} J_\Theta^{-1}}{V_0} = f_v^X + f_e^X + f_b^X$
Specific Volume of the Electrolyte	$V_e = V_{e0}\left(v_H \gamma + v_C(1)\right) = V_{e0}\left(1 + v_H(\gamma - 1)\right),$
Void Volume Fraction Evolution Per Reference Volume	$\dot{f}_v^X = C_1 \dot{v}_H f_v^X \left(J_M - 1\right)^p \operatorname{sign}\left(J_M - 1\right)^{p-1}$
Phase Transition Kinetics	if $\quad \Theta < \Theta_{MELT} - \frac{\Theta_{MW}}{2}, \qquad v_H = 0,$ elseif $\quad 2\lvert\Theta - \Theta_{MELT}\rvert \leq \Theta_{MW},$ $\quad v_H = \frac{\Theta - \Theta_{MELT} + \Theta_{MW}/2}{\Theta_{MW}},$ else $\quad v_H = 1$
Phase Fraction Conservation	$v_C + v_H = 1$
Isochoric Rate of Plastic Deformation	$\overline{\boldsymbol{D}}^X = \frac{C_2 \lvert \dot{f}_v^X \rvert}{\mu} \boldsymbol{C}^M \boldsymbol{S}_{dev}^M \boldsymbol{C}^M$
Mechanical Second Piola-Kirchoff Stress	$\boldsymbol{S}^M = \left(v_C \mu_C[J_M, \Theta] + v_H \mu_H[J_M, \Theta]\right) J_M^{-\frac{2}{3}} \left(\mathbf{1} - \frac{\mathrm{tr}\boldsymbol{C}^M}{3} \boldsymbol{C}^{M-1}\right)$ $\ldots + \left(v_C \frac{\partial \mu_C}{\partial J_M} + v_H \frac{\partial \mu_H}{\partial J_M}\right)\left(\bar{I}_{1M} - 3\right) J_M \boldsymbol{C}^{M-1}$ $\ldots + \left(v_C \kappa_C[\Theta] + v_H \kappa_H[\Theta]\right)\left(J_M^2 - 1\right) \boldsymbol{C}^{M-1}$

Table 3.3. Summary of Mechanical Model Parameters

Chapter 4

Constitutive Model Numerical Implementation

We discuss the algorithm to integrate the constitutive model through time. There are two use cases of the model as mentioned in the introduction. First, the model may be used under electrolyte transport-free conditions. That is, the mass of electrolyte per unit reference volume does not change throughout the simulation. This condition occurs within the separator only data in section 2. The second use case involves coupled poro-mechanics, in which the mass of electrolyte per unit reference volume of the material changes due to the electrolyte species migration. In this second use case, the constitutive model provides at minimum the permanent shape change of the binder along with its stress response and the volume change associated with the loss of void space, thermal expansion, and change of specific volume of the electrolyte. This latter usage of the model has not yet been explored and is discussed later in the section on future work.

Under electrolyte transport-free conditions, the constitutive model involves both thermal and kinematic inputs. The time integration algorithm proceeds as follows:

1. At $t = 0$, Initialize material properties and state variables
2. Input Θ_n, Θ_{n+1}, $\boldsymbol{F}_n$, and $\boldsymbol{F}_{n+1}$ (at t_n and t_{n+1})
3. Advance the electrolyte phase transition kinetics via one of three methods:
   (a) Input the $(v_H)_{n+1}$ and $\dot{v}_H$ from kinetics computed in a separate (energy balance) code.
   (b) Compute $(v_H)_{n+1}$ and $\dot{v}_H$ from eqs. 3.23 and 3.24, which corresponds to a linear interpolation of the phase decomposition over a finite temperature width about the melting point.
   (c) Compute $(v_H)_{n+1}$ and $\dot{v}_H$ from eqs. 3.24, 3.25, and 3.29, which corresponds to a reaction-type representation of the phase transition process.
4. Compute the deformation gradient due to thermal expansion, $\boldsymbol{F}_\Theta$ and J_Θ, from Eq. 3.22 at time t_{n+1}.
5. Compute the mechanical deformation gradient, $J_m = \det\boldsymbol{F}^M$, the non-mechanical and non-thermally expanded volume ratio, $J_X = \det\boldsymbol{F}^X$, and volume fractions of the void, electrolyte, and binder per unit reference volume (f_v^X, f_e^X, and f_b^X) and current volume at time t_{n+1} using

eqs. 3.10, 3.12, 3.20, 3.21, and 3.30. This update involves a Newton-Rhapson scheme to determine J_M, f_v^X, and J_X from which the remaining quantities may be computed.

6. Determine the instantaneous shear and bulk moduli, $\mu[\Theta, J_M]$ and $\kappa[\Theta]$ at t_{n+1}

7. Update the mechanical Second-Piola Kirchoff stress tensor, $\boldsymbol{S}^M$, from Eq. 3.14 and the isochoric plastic deformation gradient associated with the permanent shape of the binder, $\overline{\boldsymbol{F}}^X$, from Eq. 3.32. These two tensors are highly coupled and depend on $\dot{f}_v^X$. Although desired, a Newton-Rhapson scheme proved difficult to implement. Instead, an iterative scheme was implemented which proceeds as follows:

   (a) Initially, set $\overline{\boldsymbol{F}}_k^X = \overline{\boldsymbol{F}}_n^X$ and compute $\boldsymbol{S}_k^M$ corresponding to iteration k.

   (b) Do While $(\boldsymbol{S}_{dev}^M : \boldsymbol{S}_{dev}^M)_k - (\boldsymbol{S}_{dev}^M : \boldsymbol{S}_{dev}^M)_{k-1} > 10^{-10}$

      i. Set $k \to k-1$

      ii. Compute $\boldsymbol{F}_k^M$ from $\boldsymbol{F}_{n+1}$ and $\overline{\boldsymbol{F}}_{k-1}^X$

      iii. Compute $(\boldsymbol{S}_{dev}^M)_k$ and $(\boldsymbol{S}_{dev}^M : \boldsymbol{S}_{dev}^M)_k$

      iv. Compute $(\overline{\boldsymbol{L}}^X)_k$ and update $\overline{\boldsymbol{F}}^X$ to iteration k

   (c) Set $\overline{\boldsymbol{F}}_{n+1}^X = \overline{\boldsymbol{F}}_k^X$ and $\boldsymbol{S}_{n+1}^M = \boldsymbol{S}_k^M$

8. Compute the Cauchy stress, $\boldsymbol{\sigma}_{n+1} = J_M^{-1} \boldsymbol{F}_{n+1}^M \boldsymbol{S}_{n+1}^M (\boldsymbol{F}_{n+1}^M)^T$

9. Store state variables

10. In a coupled thermal-mechanical analysis, compute the heat capacity per current volume as the pushforward of Eq. 3.17, and return it along with the structural elastic heating and dissipation due to volumetric and isochoric plastic flow.

Item 7 requires two additional comments. It is worth noting that because $\det\left(\bar{\boldsymbol{F}}^X\right) = 1$ by definition of an isochoric deformation gradient, ($\bar{\boldsymbol{F}}^X \in SL(3)$), numerically accurate incremental updates of $\bar{\boldsymbol{F}}^X$ in item 7 involve the exponential map. See reference for further information [19]. Second, the iterative scheme typically exhibits a first order convergence rate so that typically 10-15 iterations are required to meet the tolerance. However, if too large of a time step is taken, then the scheme may not converge, and the implemented model issues a request to cutback the time step. The maximum time step in which the model may converge has not yet been found, and is currently estimated based on an explicit time integration scheme, but this approach is not conservative. The satisfaction of the basic multiplicative split of the deformation gradient kinematics, Eq. 3.3, at time t_{n+1} was checked during the rate of convergence studies and found to be satisfied even more stringently than the tolerance on deviatoric stress norm increments. Hence, we conclude that this iterative scheme results in an implicit time integration of item 7 and thus the entire constitutive model.

Note that the balance laws and thermodynamics concepts used in this report are included in the appendix. They do not represent new contributions.

Chapter 5

Separator Material Calibration

A strength of the constitutive modeling approach in section 3.3 is that it can be calibrated directly from macroscale data for the electrolyte flow-free condition. That is, thermal expansion, specific volume change of the electrolyte, shear and bulk moduli and their thermal and deformation dependencies, and evolution rules for the loss of porosity and isochoric plastic deformation can all be calibrated from data presented in section 2. When electrolyte transport is considered, the interpretation of the material properties in the model may change, and so too would the calibration procedure. This latter topic is discussed later in the section on future work.

Beginning with mechanical data, we note that Poisson's ratio measurements at room temperature of the separator were $\nu = 0.003 \approx 0$ [18]. Then, turning to the oscillatory shear measurements, we determine the shear modulus and its temperature and hydrostatic compression dependencies from Fig. 2.2. Cold state properties are references to 50C, and hot state properties are referenced to 500C. Temperature dependencies of the shear modulus in the cold and hot states are approximated as linear. We further assume that the bulk modulus in the cold and hot states has the same temperature scaling as the shear modulus such that the poissons ratio at small deformation does not change with temperature.

We assume that the bulk modulus does not change with hydrostatic compression, but the shear modulus does. Its dependence on hydrostatic compression requires additional approximation of the available data in Fig. 2.2 because, as implemented in the constitutive model, the shear modulus depends on the engineering volume strain, $\mu = \mu[J_M - 1]$. We assume that the axially applied compressive stress in Fig. 2.2 subjects the separator pellet to a state of uniaxial stress with superimposed torsion. Thus, the hydrostatic compressive stress is $\frac{\boldsymbol{\sigma}_{\text{applied}}}{3}$, which is linearly related to the volume strain through the known bulk modulus. Above the melting transition, we do not have bulk modulus data, but we continue to assume that the Poisson's ratio, which may be reasonable under small deformation and slow loading rate conditions (so that the molten electrolyte has time to flow, which reduces its contribution to the stress at the microscale).

Finally, we use the melting temperature from the literature, which is confirmed experimentally in Fig. 2.2 as well as the specific volume change of the pure LiCl-KCl electrolyte on melting. We do not currently exercise the thermal heat capacity capabilities of the model as these parts are handled in an energy balance ARIA module. For the simulations performed here, the temperature distribution is assumed to be uniform and correspond with the controlled environmental temperature. Model parameters under the flow free conditions, with the exception of the void fraction

evolution rule and isochoric plasticity are reported in table 5.

Parameter	Unit	Value	Parameter	Unit	Value
Θ_{MELT}	K	625	Θ_{MW}	K	10
Θ_{C0}	K	300	Θ_{H0}	K	773
$\Theta_{\alpha 0}$	K	300	α_C	K^{-1}	40E-6
α_H	K^{-1}	10E-6	γ	none	0.2
κ_{C0}	MPa	22.55	μ_{C0}	MPa	33.81
κ_{C1}	MPa K^{-1}	0.050	μ_{C1}	MPa K^{-1}	0.076
κ_{H0}	MPa	12.69	μ_{H0}	MPa	19.04
κ_{H1}	MPa K^{-1}	0.072	μ_{H1}	MPa K^{-1}	0.11
f_{v0}	none	0.25	f_{s0}	none	0.57
f_{MgO0}	none	0.18			

Table 5.1. Calibrated separator material parameters I

5.1 Non-Mechanically Driven Void Fraction Evolution

Three parameters remain to be calibrated: C_1, p, and C_2. The first two control the phenomenological void fraction evolution determined through Eq. 3.30 while C_2 determines the amount of concomitant isochoric plasticity (shape change) from Eq. 3.32. In the simplest calibration, one assumes that the evolution of void fraction is not mechanically driven, which implies that the volume fraction of voids is the same for all applied stresses to the separator as it is heated through the electrolyte melt transition. This behavior is realized through selecting $p = 0$. Then, the parameters C_1 and C_2 are fit such that the model best reproduces engineering axial (height) strain change across the melting transition. Comparisons of the fit axial and predicted transverse (diameter) strain changes are shown below using the same data from Fig. 2.4 under assumed uniaxial stress conditions. This latter assumption is important to the model calibration as will be discussed in subsequent sections on that examine the fully confined uniaxial strain behavior.

	p (none)	C_1 (none)	C_2 (none)
Non-Mechanically Driven (Stress-Free BC)	0	7	492
Mechanically Driven (Stress-Free BC)	1	1000	315
Mechanically Driven (Bonded BC)	1	1145	600

Table 5.2. Calibrated separator material parameters II: Void fraction and plasticity parameters. Note, all are dimensionless and phenomenological.

Using this calibration under uniaxial stress conditions, the model is capable of fitting the compaction behavior of the separator across the melt transition. The transverse strain behavior is reasonably fit for half of the data available. However, the data at 8 and 10 psi is not consistent with a net volume change of approximately 10%. See Fig. 2.5 and subsequent relevant discussion. Instead Fig. 5.1 shows a net volume change of approximately 12 % is observed at 8 and 10 psi axial loads. Since this form of the constitutive model is not capable of producing different volume strains under different applied stresses, it cannot represent this changing behavior.

Multiple mechanical processes occur during the melting of the electrolyte, so it is worthwhile to examine the time histories of strain and volume fraction quantities across the electrolyte melting transition. Under stress free conditions, this form of the model compacts across the melting transition with the diameter and height strains being equal in Fig. 5.2(a) and both negative. However, at 15 psi in Fig. 5.2(b), the pellet has compacted axially and expanded outward, still with a volume change of approximately 12% across the transition. Figures 5.2(c) and 5.2(d) show the mechanical ($J_M - 1$), non-mechanical ($J_X - 1$), and net volume change histories ($J - 1$) at 0 and 15 psi respectively. Thermal expansion strains are not included in ($J_X - 1$) but are in the net volume change history; hence, these curves do not overlay. Prior to melting, thermal expansions is significant, but as the electrolyte starts to melt, the specimen compacts rapidly and spherically at 0 psi and with substantial shape change at 15 psi until the void fraction ceases to diminish. Because the void fraction evolution is independent of applied stress, the non-mechanical volume change, ($J_x - 1$), is the same in figs. 5.2(c) and 5.2(d). A slight difference in mechanical and net volume changes between the two figures especially after the melt transition.

At this point, all of the curves in Fig. 5.2, show conspicuous minima followed by a slight increase. This minimum is simply a consequence of the phase transition and void fraction evolution processes evolving under different time scales. Recall that the phase transition kinetics are represented as a linear interpolation between the hot and cold states across a 10 C temperature range about the melting temperature. Hence, the void fraction evolution completes before the phase transition has completed. Because the electrolyte expands by 20% on melting, the net volume and non-mechanical volume changes reverse direction until the phase transition completes. The onset

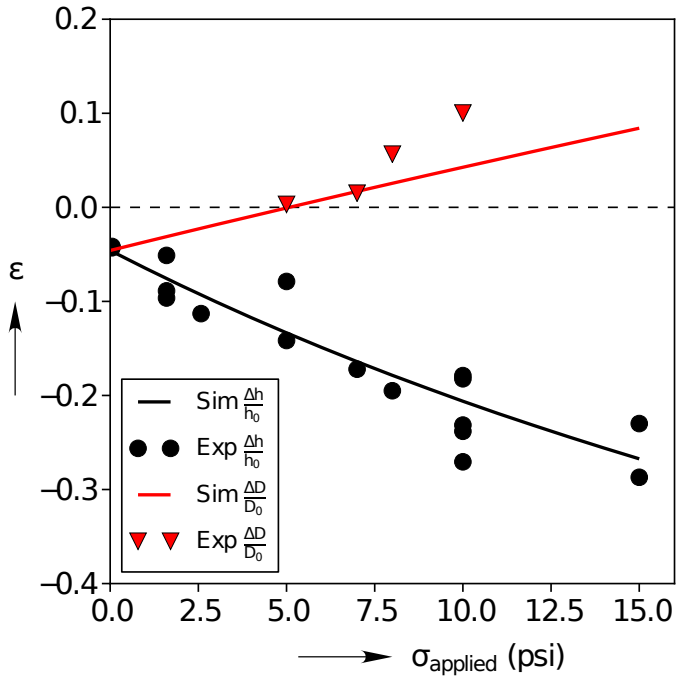

Figure 5.1. Separator model fit of the axial strain change across the electrolyte melting transition using $p = 0$, $C_1 = 7$, $C_2 = 492$ dimensionless material parameters

of the plateau marks the end of the electrolyte phase transition. These minima are likely artifacts of the model that arise because of the specific form of the void fraction evolution rule. Hence, if a different rule is used to diminish the void fraction, they will change.

5.2 Mechanically Driven Void Fraction Evolution

Next, we calibrate the model to the axial strain change on electrolyte melting under the condition when the loss of void volume fraction is linearly related to the hdyrostatic mechanical volume strain, $(J_M - 1)^1$ in which $p = 1$. Again assuming uniaxial stress conditions, the parameters that best fit the axial strain data are $C_1 = 1000$ and $C_2 = 315$. The comparison between the axial and transverse strains are shown in Fig. 5.3.

Now, at 0 psi axially applied stress, there is no void evolution since $J_M - 1 = 0$. Without void evolution, there is also no isochoric plasticity, so that across the phase transition, the only phenomenon that is observed is the expansion of the electrolyte. Hence, the volume expands by 11.4% rather than contracting. This behavior is not expected to be observable since there will always be capillary pressure between the electrolyte and MgO binder such that, in batteries, a compressive pore pressure will be present. As the applied stress increases, the model is able to

represent the axial strain data at higher applied stresses although agreement of the transverse strain data between experiments and predictions is qualitative only.

With $p = 1$, the model predicts that the net volume continues to decrease with applied stress, but experimentally, it is not clear whether this is the case. See Fig. 2.5. Consequently, the loss of void volume fraction changes with applied stress levels, which is easily seen by examining the void volume fraction change (in the current configuration) across the transition. Here we normalize the void volume fraction to its initial value of 25% by volume in Fig. 7.3. Note that although the void volume fraction does not evolve under stress free conditions in the reference configuration ($J_M - 1 = 0$), the void volume fraction has changed at 0 psi in the current configuration. However, this change is simply due to the expansion of the electrolyte and rebalancing of the void, binder, and electrolyte volume fractions to sum to unity in the current configuration. As the applied axial stress increases, the normalized change in void volume fraction decreases significantly such that by 8 psi deadload, less that 80% of the normalized void volume fraction remains.

We now examine the time histories of strain components, volume strains, and constituent volume fractions at 0, 5, and 15 psi to examine how the model behavior changes with increased applied stress. Again, a volume increase is observed at 0 psi due to the electrolyte expansion on melting. By 5 and 15 psi applied stresses, the net volume change across the melt transition is negative as the pellet compacts and expands outwards. Compared with simulations using $p = 0$, no fictitious minima are observed in the strain histories, because, with $p = 1$, the void fraction evolution varies continuously with the mechanical volume strain and the phase transition kinetics. Hence, the void fraction diminishes and isochoric plasticity occur over the entire phases transition rather than for just a part of it. See Fig. 5.3 for comparison. Fig. 5.6 shows that the volume non-mechanical volume strain, $J_X - 1$, changes singificantly across the melt transition with increased applied stresses. The mechanical volume strain, by comparison, is always small, and the net volume strain transitions from positive to negative as discussed. The behavior of the non-mechanical (and non-thermal) volume strain is more easily seen by examining the volume fraction decomposition of the electrolyte, binder, and void space constituents in the current configuration.

Since the model considers that thermal expansion applies equally to all phases, the volume fractions of different constituents only change during the electrolyte melt transition. As the void volume fraction diminishes and electrolyte phase expands, the volume fraction of the electrolyte will always increase. However, the volume fraction of the binder phase decreases if not enough void space is lost, see Fig. 5.7(a) but increases at higher applied stresses, see figs. 5.7(b) and 5.7(c). These results may be important when this model is applied in a poro-mechanics environment in which the volume fraction of the binder phase may directly relate to that phase's thermal-mechanical behavior.

Without questioning the assumptions of uniaxial stress or electrolyte flow-free conditions, the weakness of this modeling approach (with $p = 1$) is that it cannot represent the low applied stress compaction behavior of the separator pellet. Fundamentally, we know that capillary pressure is active when the electrolyte melts, and that the fluid response is important to the mechanics of the composite material. Here, we examine the effects of a fictitious capillary pressure, applied as a hydrostatic pressure of 5 psi during the electrolyte melt transition, and look at the axial and transverse changes in strain across the melt transition, which are reported in Fig. 5.8. No effort has

been made to re-calibrate the model. That is $p = 1$, $C_1 = 1000$, and $C_2 = 315$ with the additional 5 psi hydrostatic (fictitious capillary) pressure, which was chosen to be in the middle of the range of axially applied stresses. The model now reproduces the low applied stress compaction behavior seen experimentally in Fig. 5.8 and hence reasonably fits the height strain data across the 0-15 psi axially applied stress range. As expected, the void fraction evolution changes at the lower applied stresses due to the presence of the 5 psi fictitious hydrostatic pressure although these results are not included. The quality of the predicted diameter strains remains unaffected by the added hydrostatic pressure. From this brief exercise, we conclude that inclusion of the effects of capillary forces allows the model to properly compact as the electrolyte melts over the range of stresses for which we have data.

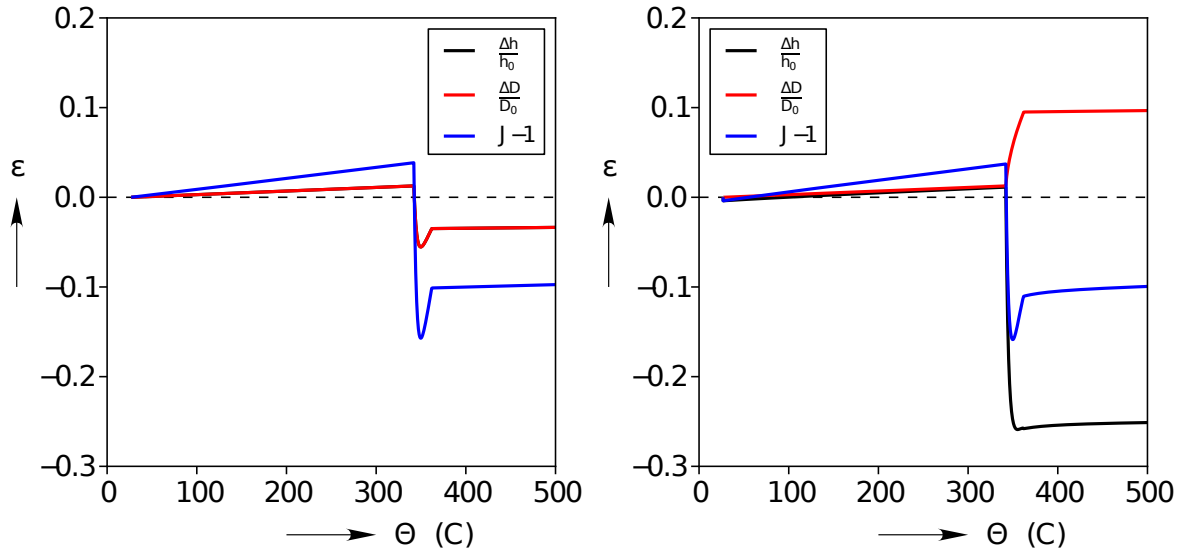

(a) Strain history for $p = 0$ and at 0 psi applied stress. **(b)** Strain history for $p = 0$ and at 15 psi applied stress The height and diameter strain curves are coincident

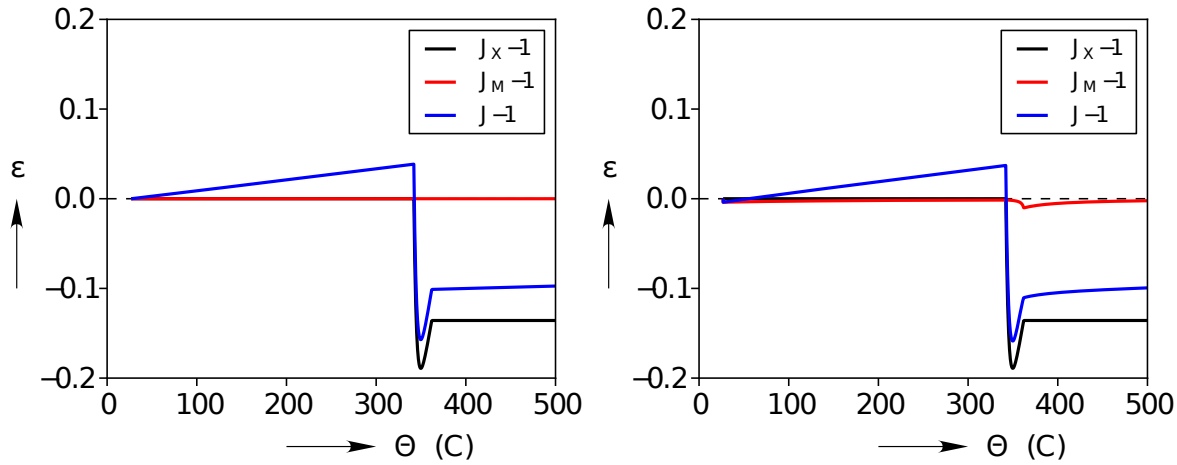

(c) Volume strain histories for $p = 0$ and at 0 psi applied stress

(d) Volume strain histories for $p = 0$ and at 15 psi applied stress

Figure 5.2. Strain histories of separator pellets subjected to 0 and 15 psi for $p = 0$

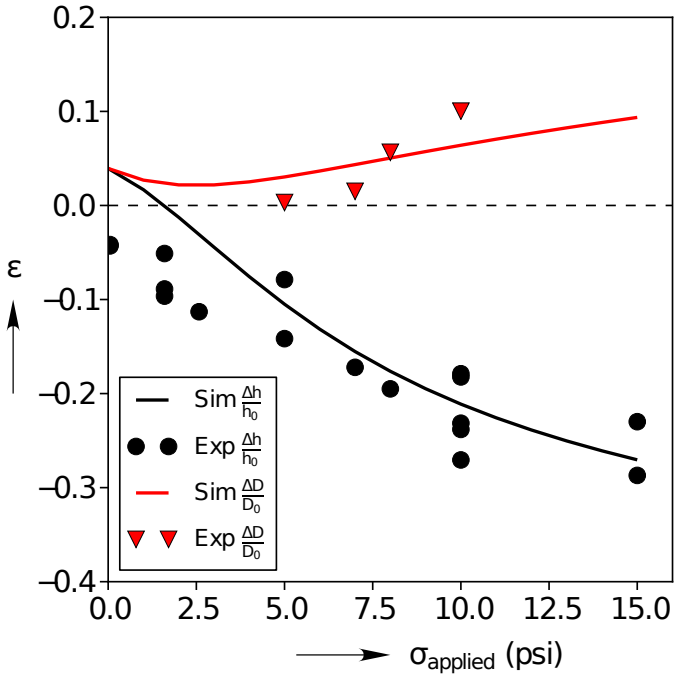

Figure 5.3. Separator model fit of the axial strain change across the electrolyte melting transition using $p = 1, C_1 = 1000, C_2 = 315$ dimensionless material parameters

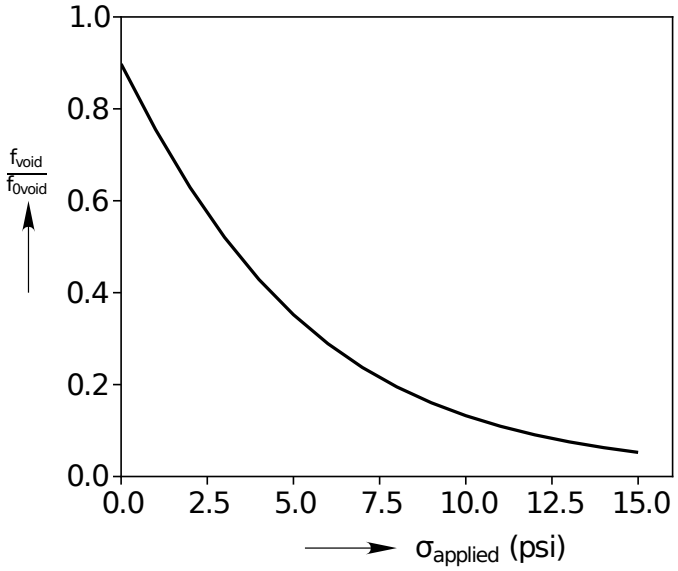

Figure 5.4. Change in the current configuration void volume fraction across the melt transition normalized by the initial 25% by volume void fraction.

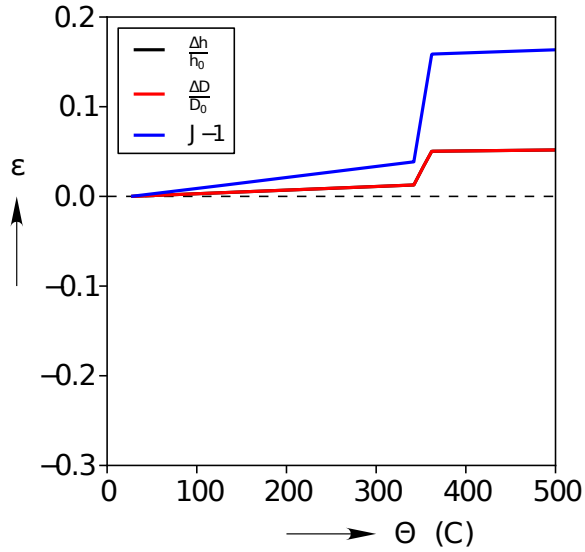

(a) Strain history for $p = 1$ and at 0 psi applied stress. The height and diameter strains histories are coincident.

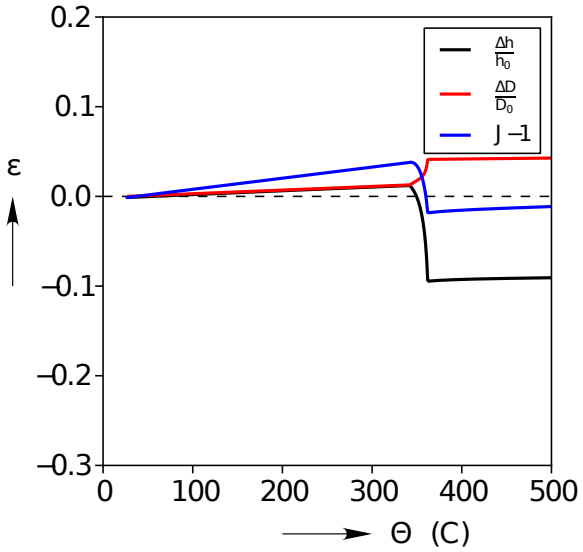

(b) Strain history for $p = 1$ and at 5 psi applied stress

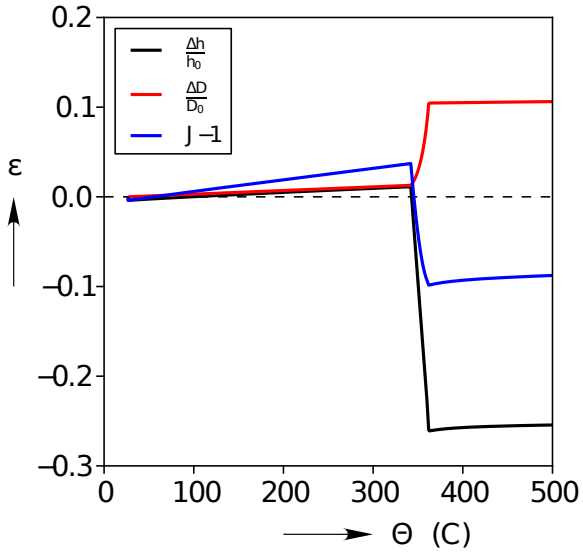

(c) Strain history for $p = 1$ and at 15 psi applied stress

Figure 5.5. Strain histories of separator pellets subjected to 0, 5, and 15 psi axial stress for $p = 1$

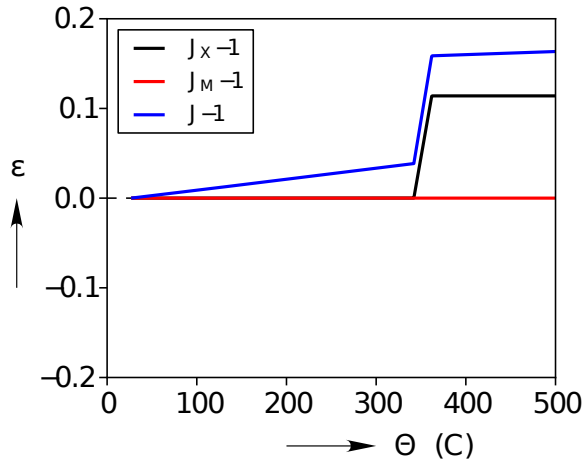

(a) Volume strain histories for $p = 1$ and at 0 psi applied stress

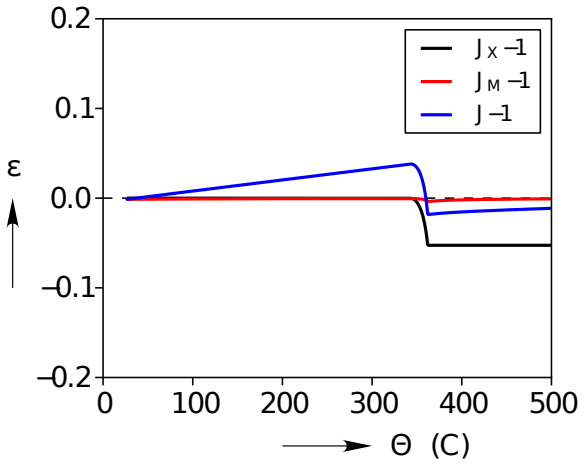

(b) Volume strain histories for $p = 1$ and at 5 psi applied stress

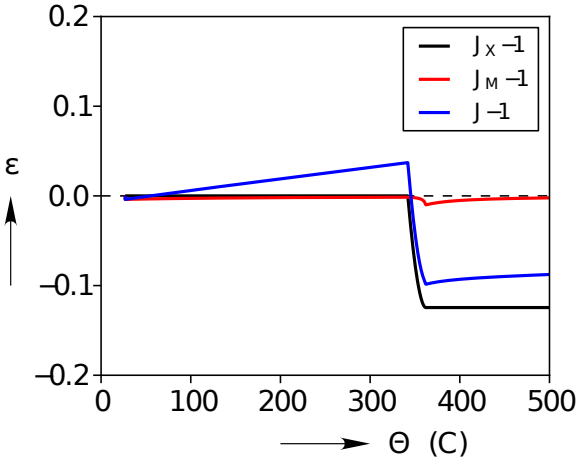

(c) Volume strain histories for $p = 1$ and at 15 psi applied stress

Figure 5.6. Volume strain histories of separator pellets subjected to 0, 5, and 15 psi for $p = 1$

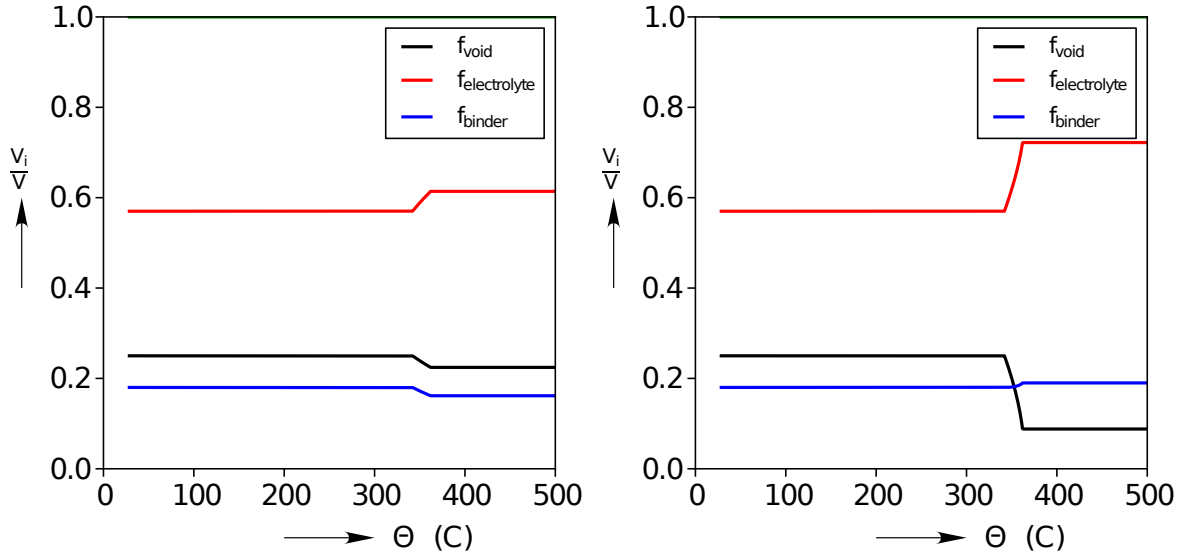

(a) Volume fraction histories for $p = 1$ and at 0 psi applied stress

(b) Volume fraction histories for $p = 1$ and at 5 psi applied stress

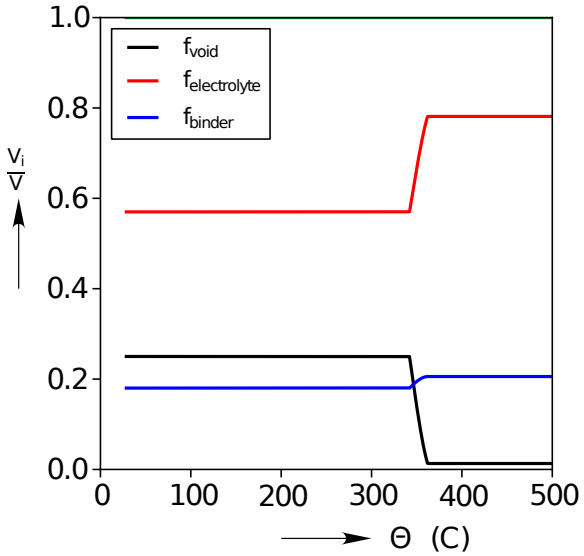

(c) Volume fraction histories for $p = 1$ and at 15 psi applied stress

Figure 5.7. Current configuration volume fraction time histories of the void space, electrolyte, and binder within separator pellets subjected to 0, 5, and 15 psi at $p = 1$

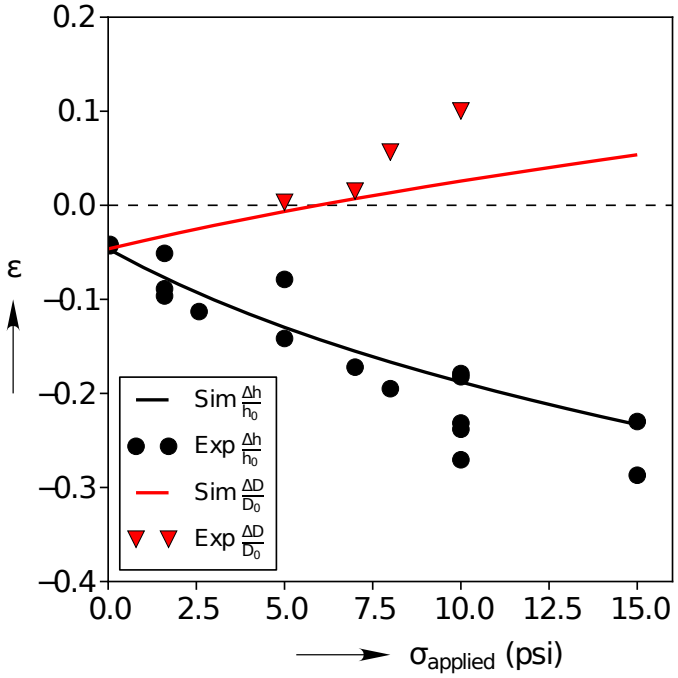

Figure 5.8. Axial and transverse strain changes across the melting transition with $p = 1$, $C_1 = 1000$, $C_2 = 315$ and a 5 psi fictitious capillary pressure.

Chapter 6

Separator Model Validation

The applied axial stress dead loads are not representative of the mechanical environment in which separators, anodes, and cathodes are used within thermal batteries during fire-up. Typically, batteries are packaged under a fixed closing force through the compression of insulation layers at the top and bottom of the stack of electrochemical cells [20, 10]. When the batteries fire-up and the electrolyte melts, the separator (and to a lesser extent the cathode) inelastically compress as the insulation layers mechanically unload [10]. Thus, validation of this constitutive model should involve a spring-like boundary condition. Typical insulation materials used in thermal batteries, such as fiber frax board and MinK show complex, history dependent mechanical responses [13], so instead of using such materials, we selected stainless steel wave springs from Smalley Steel Ring Co. Specifically, CM06S17 and CM08S17 waves springs where used; specs for these springs can be found on the manufacturers website [3]. The wave spring characterization and fit of these springs at room temperature and 350 C are shown in Fig. 6.1. Note that the loading curve is fit since we are ignoring effects of friction and creep in the springs which may cause the hysteresis seen at 350 C in both springs. Note that the manufacturer warned that these springs could show creep above 300 C, which we observed through the development of an inelastic strain of less than 1% strain in thermal cycles between 300 and 400 C. This behavior and friction of the spring against the platens may explain the slight hysteresis observed in the 350 C curves. We neglect these effects and treat the springs as elastic as shown by the fit curves in Fig. 6.1.

A photograph of the validation test setup is shown in Fig. 6.2. The tests were performed in the ARES 2 rheometer and proceeded as follows. The separator pellet (6mm diameter, 1 mm height) was placed on the steel platens followed by a sapphire disc followed by the waves spring and the upper platen. The assembly was brought up to 300 C, and held for a period of time for thermal equilibration. Then, a compressive load was applied, and the displacement then held fixed. The temperature was then brought up at a rate of 2C per minute to 375C, which is beyond the melt transition of the electrolyte. The quantity of interest in these tests is the final load experienced by the structure after the electrolyte melts, the separator compacts, and the wave spring elastically unloads.

As with the calibration in sections 5.1 and 5.2, boundary conditions are important. We continue with our uniaxial stress approximation so that previously calibrated material parameters can be used, and we continue to assume electrolyte flow-free conditions. Thus, to model this assembly, we consider three material blocks that correspond to the wave spring, which is represented as a linear elastic disc 6 by 10 mm diameter to height, a 6 x 1 mm diameter to height sapphire disc,

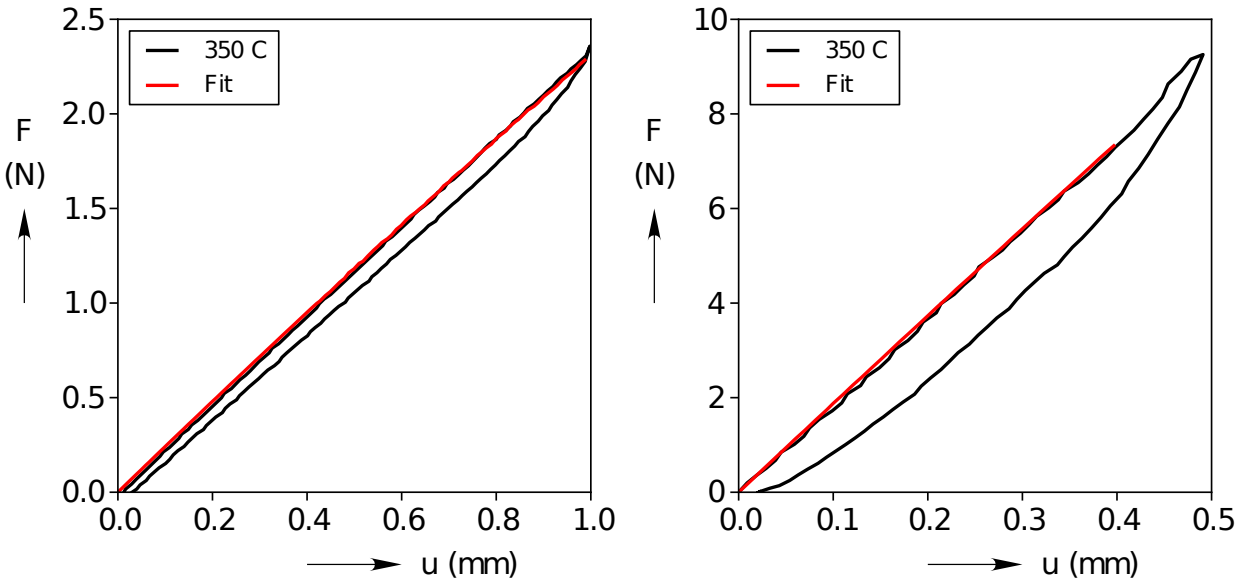

(a) CM06S17 Wave spring characterization and fit

(b) CM08S17 Wave spring characterization and fit

Figure 6.1. Wave spring characterization at room temperature and 350C and fits at the latter temperature. 06 and 08 indicate the outer diameter of the springs, which determines the difference in stiffnesses.

and a 6 by 1 mm diameter to height separator pellet. To fit the data in Fig. 6.1, the isotropic elastic constants were $E = 0.857$ MPa and $\nu = 0$ and $E = 6.67$ MPa and $\nu = 0$ for the CM06S17 and CM08S17 wave springs respectively. The 10 mm wave spring disc thickness was chosen to insure that the spring response is linear over the deformation response in these tests. Sapphire is approximated as an isotropic elastic solid with a Youngs and shear modulus of 345 and 145 GPa respectively [4]. Given the substantial mismatch in stiffness between the sapphire and either the separator or wavespring, the deformation in the sapphire layer is negligible; hence the isotropy approximation is reasonable.

Uniaxial stress is achieved through frictionless boundary conditions between the different layers. Under such conditions, only one element per material block is needed. Uniform gradient, linear hexahedral elements are employed in an implicit quasi-static analysis in which the temperature field is considered uniform and is directly applied. Computationally, we follow the same steps as the experiment and predict the net force response vs. time for separator pellets under the action of the two springs. The results associated with the two model calibrations corresponding to $p = 0, 1$, $C_1 = 7, 1000$, and $C_2 = 492, 315$ are shown in Fig. 6.3. Capillary pressure effects were not considered. The experimental results show a distinct decline in the force response of the assembly below the melt transition of the electrolyte. In both cases, the force diminishes by approximately 10% relative the starting value of each test. The mechanism for this force decline is under investigation and is thought to be high temperature creep of the solid electrolyte, a mechanism that is likely not important in thermal batteries which are heated from room temperature

Figure 6.2. Wave spring validation test setup within the ARES 2 rheometer. The wave spring, sapphire plate, and separator pellet are visible in ascending order between the stainless steel platens.

to roughly 500 C in less than one second. There also appears to be (PID) control issues associated with maintaining a fixed displacement as evidenced by the periodic variations in the test data. Wave spring creep is not thought to cause the significant load drop observed in the tests.

By comparison with the experimental data, both calibrations of the model show an increase in the force response of the assemblies due to thermal expansion of the electrolyte prior to the electrolyte melting. Note that thermal expansion of the wave springs and sapphire disks is neglected. across the transition, a precipitous drop in the force response of the structure is observed by both the experiments and the two model calibrations. For the more compliant spring, CM06S17, both calibrations produce more of a net force change than the experiment and are similar to each other. This latter result is sensible since the hydrostatic stress within the separator does not change significantly during the load drop for the CM06S17 scenario. Hence, the $p = 0$ and $p = 1$ responses should be similar.

In contrast, for the CM08S17 experiment, the two different calibrations are distinct. The $p = 0$ calibration predicts the final load response of the structure very well while the $p = 1$ calibration predicts a slightly larger remaining load than is seen experimentally. The difference of the two models is expected because the $p = 1$ void fraction evolution and isochoric plasticity are tied to the mechanical volume strain $J_M - 1$. Hence, as the net load diminishes substantially, the rate of void fraction evolution and plastic shape change diminishes while such behavior does not occur for $p = 0$. As with the axial dead load experiments during calibration, the $p = 0$ calibration shows an artificial load minimum again due to the void fraction evolution (and concomitant plastic shape change) completing before the phase transition is complete. Hence, there is a period of time in which the electrolyte expands without accompanying change void fraction or shape, which cause the load to increase. This response is not observed experimentally. Overall, the constitutive model is able to represent the compaction behavior of the separator under the validation test-spring

like boundary conditions relevant to battery applications assuming uniaxial stress, elastic spring behavior of the wave spring, and electrolyte flow-free conditions.

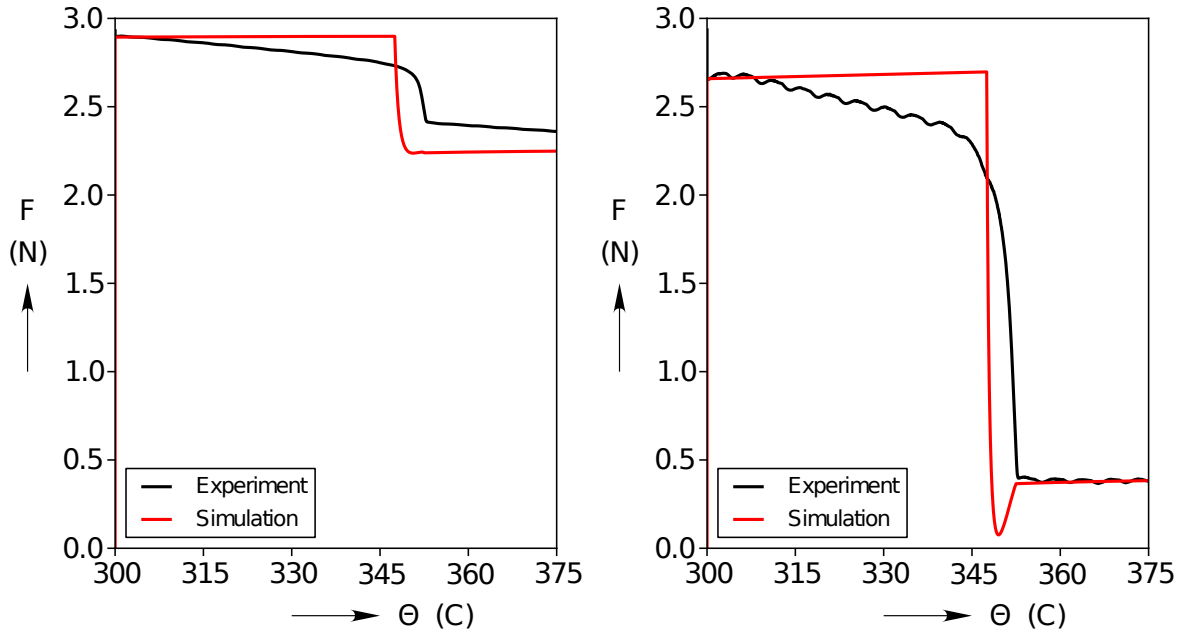

(a) CM06S17 Wave spring test and model prediction ($p = 0$)

(b) CM08S17 Wave spring test and model prediction ($p = 0$)

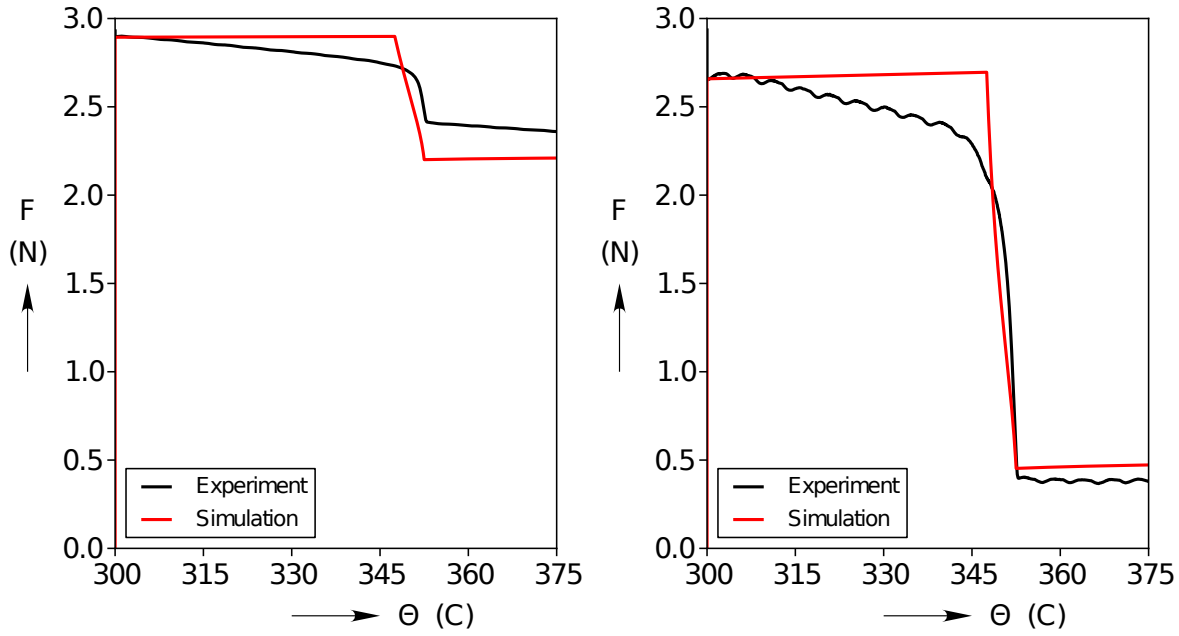

(c) CM06S17 Wave spring test and model prediction ($p = 1$)

(d) CM08S17 Wave spring test and model prediction ($p = 1$)

Figure 6.3. Wave spring validation test results and predictions for the two calibrated instances of the model $p = 0, 1$

Chapter 7

Fully Confined Boundary Conditions

An assumption in the previous sections has been that the pellets are subjected to states of uniaxial stress, which implies frictionless boundary conditions between the separator and surrounding materials. This interaction may not reasonable in batteries because pellet materials may interact through traditional asperity contact as well as through molten electrolyte capillary effects (in the hot state of the materials). The experimental data considered in this report do not include a laterally applied radial stress, but they do involve a 6:1 diameter to height aspect ratio pellets in contact with stainless steel platens. In reality, we do not yet know what the boundary conditions are between the different layers, so in this section, we consider a strong (bonded) interaction between the separator and the surrounding platens, which represents the opposite extreme from the frictionless (uniaxial stress) conditions. We consider the same calibration and validation experiments with the boundary condition, which requires 3D simulation.

First, the parameters C_1 and C_2 responsible for void loss and isochoric plasticity must be re calibrated to fit the height data with the bonded boundary conditions. Notice, from Fig. 2.4(b) that at 5 and 7.5 psi axially applied stresses, the diameter strain across the electrolyte melt transition is nearly zero, which suggests that the separator pellet compacts axially in an approximate state of uniaxial strain. We take advantage of this observation and calibrate the model (again with $p = 1$ and without capillary pressure due to the fluid) by choosing $C_1 = 1145$ and $C_2 = 600$ to fit the 10-12% axial engineering strain change on electrolyte melting at 5 psi axially applied stress. Then, with these parameters, we simulate full 3D separator pellets bonded to steel platens over the range of axially applied pressures from 0 to 15 psi at an increment of 1 psi.

The finite element representation of this problem is as follows. We consider the axially symmetric $r-z$ half plane by making symmetry cuts through the center of the separator across its axis and by considering the behavior of a 2 degree slice (rather than the full circumference of the discs). The separator pellet and stainless steel platens are meshed with linear hexahedral bricks of a specified characteristic size in the $r-z$ plane and with 1 element through the thickness in the hoop (θ) direction. The uniform gradient (reduced integration) scheme is used to compute to integrate element fields. A schematic of the finest mesh considered is shown in Fig. 7.1 with applied boundary conditions. Approximately 1000 elements are employed with 10 elements along the axial direction of the separator. Note, the imposed axial symmetry condition (hoop direction) is not shown. Simulations were performed in an implicit quasi-statics module of the SIERRA Solid Mechanics code suite [23] using residual and relative residual tolerances of 1.0E-8. Meshes were generated using the code CUBIT [21].

As before, a nominal stress is applied to the pellet and held while the temperature is ramped upward at 5 C/min through the melt transition. Given the bonded boundary condition between the stainless steel platen, which is treated as an isotropic elastic material with a youngs modulus and poissons ratio of $E = 200$ GPa and $\nu = 0.29$ respectively [15], and the separator pellet as well as the enormous mismatch in elastic moduli between the two materials, radial motion of the pellet bonded to the steel is negligible. The thermal expansion coefficient of the platens is assumed to be 17.8E-6 per degree C [15]. Thus, the diameter change and strain is taken as from the motion of the pellet along the z (axial) symmetry axis, which corresponds to the maximum diameter change. The axial strain is nearly uniform, so it is taken from the motion of the innermost nodes bonded to the platen. Note that an artificial hole is introduced of 1/10 the radius of the pellet to simplify the meshing and mesh quality. Taking out this material is equivalent to removing $1/100^{\text{th}}$ of the volume of the disc. We report the height and diameter strains in comparison to the experiments as well as the change in normalize void fraction across the transition as a function of applied axial stress.

We also examine the axial and radial strain fields within the separator after the electrolyte melting transition has completed. We choose three representative cases, 1, 5, and 15 psi axially applied stresses, which correspond to cases that consume a range of void space across the transition as shown in Fig. 7.3. These results are presented in Fig. 7.4.

Using these parameters, we re-run the validation simulations now under fully bonded conditions and in a 3D setting. Again, a 2 degree slice of the axially symmetric setup is considered. There are no symmetry planes along the cylinder axes as is evident from the experimental setup in Fig. 6.2, so the full 6 by 1 mm diameter to height separator layer is modeled which is bonded to a 1 mm thick sapphire disc above followed by the 10 mm thick wave springs. The sapphire is then bonded above by either the CM06S17 or CM08S17 wave springs (as represented by elastic discs; see section 6). The thermal expansion behavior of the sapphire is also considered isotropic and is taken as the maximum expansion coefficient over its different crystallographic directions at 7.7E-6 per degree C. Between 300 and 375C, thermal expansion mismatch plays a small role in this boundary value problem. Note that there is also a thermal mismatch between the separator and steel platen below. The geometry are boundary conditions depicted in Fig. 7.5. The same spring characterization and representation as previously discussed is used for the CM08S17 and CM06S17 springs. Since only a fraction of the area is considered, the net reaction force against the platens is given by the reaction for of the slice multiplied by 180. Again, 1/10 of the cylinder is not considered in the center, but this loss of 1% of the volume is not considered in the net force calculations. The comparison against experiments for these boundary conditions is, Similar strain fields are observed as in Fig. 7.4 for these validation simulations under bonded constraints and hence are not reported. Again, the majority of deformation is nearly in a condition of uniaxial strain (along the cylinder axes) with the exception of near the outer boundary of the separator.

Considering the uncertainties in the calibration dead load experiments as well as the wave spring validation experiments, refer to sections 2 and 6, we observe that all three sets of calibration and validation predictions compare reasonably well against experiments. None are able to to predict the transverse results seen experimentally, but all decently reproduce the axial strain behavior of the separator pellet across the melt transition under both dead load and spring like

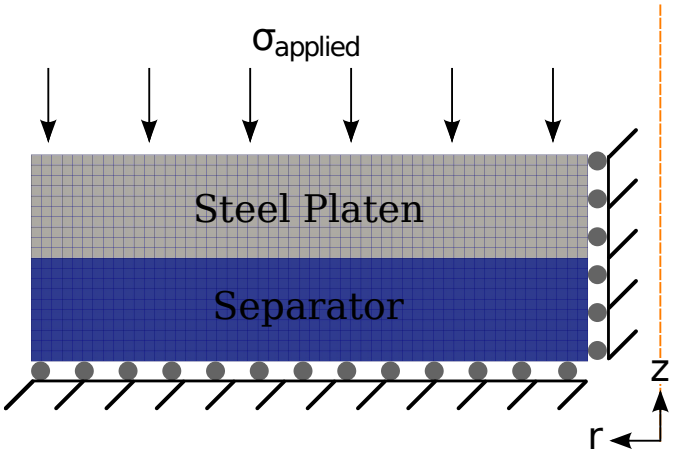

Figure 7.1. Finite element mesh and boundary conditions associated with the platen-separator-platen geometry. A 2 degree wedge is simulated with an imposed axial symmetry condition in the hoop direction, which is in and out of the image. A symmetry plane normal to the z axis (horizontally oriented rollers). The inner $1/10^{\text{th}}$ of the radius is cut out to prevent the need for tetrahedral elements or wedge elements. The orange dashed line schematically represents the line along which $r = 0$. The gray region represents the stainless steel platen while the blue region corresponds to the separator. These regions share nodes at their boundaries and hence are perfectly bonded. In the calibration simulations, the axial stress σ_{applied} is applied to the platen top. Since the platen is orders of magnitude stiffer than the separator, its deformation is negligible.

boundary conditions. The calibration and validation simulations are made with assumed boundary conditions (either frictionless and hence uniaxial stress conditions or fully bonded constraints between the separator and surrounding layers), and since the predictive capabilities of the model under these two scenarios is relatively insensitive to the choice of boundary condition, we make two conclusions. First, the time integration of the constitutive model is implemented reasonably and the model form of the plastic response and volume change of the separator is adequate to describe such experiments. Second, additional validation tests are needed to test the model over a broader range of deformations and temperature histories as well as changes to composition. Since the inelastic response does depend on the initial composition of the pellets, it is anticipated that if the initial volume fractions of electrolyte, binder, and void space are changed then additional calibration tests would be required.

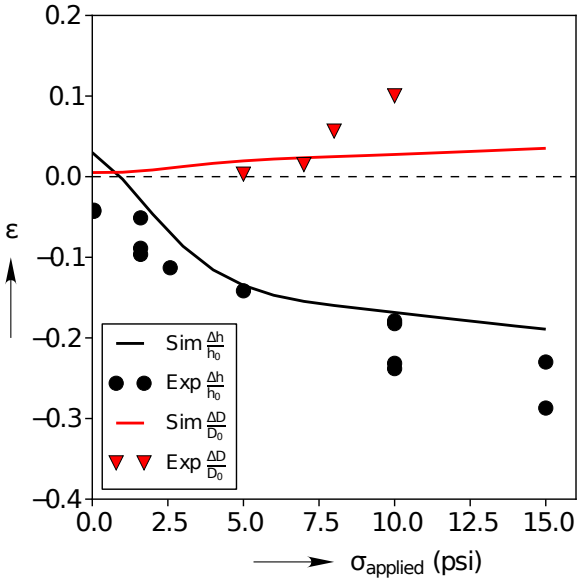

Figure 7.2. Separator model fit of the axial strain change across the electrolyte melting transition using $p = 1, C_1 = 1145, C_2 = 600$ dimensionless material parameters and perfectly bonded boundary conditions between the platen and separator

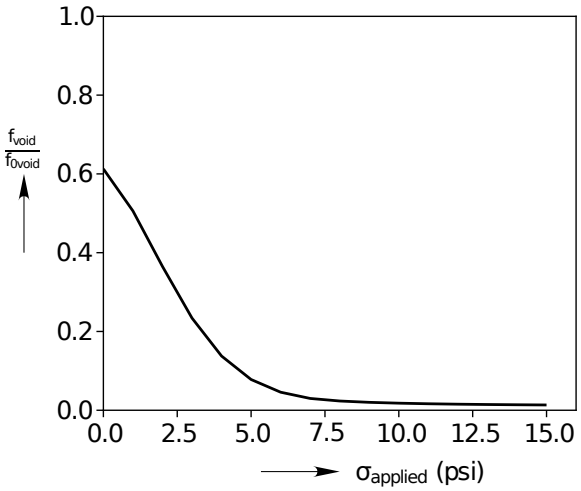

Figure 7.3. Change in the current configuration void volume fraction across the melt transition normalized to the initial volume fraction of voids. This void fraction represents and average quantity over the entire separator specimen although the field varies only near the outer radius of the cylinder.

(a) 1 psi applied stress

(b) 1 psi applied stress

(c) 5 psi applied stress

(d) 5 psi applied stress

(e) 15 psi applied stress

(f) 15 psi applied stress

Figure 7.4. Axial and radial strain fields post melting in the separator bonded to steel platens. Note that negligible strain exists within the stainless steel platens. All strains are logarithmic which approximately engineering strains at these magnitudes.

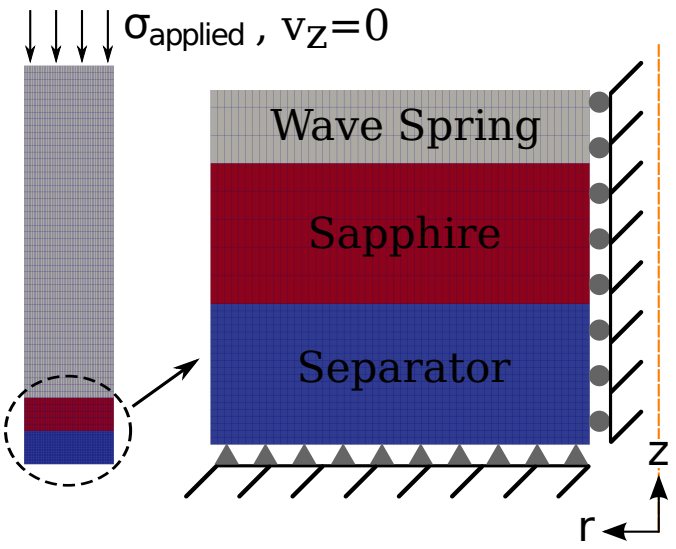

Figure 7.5. Finite element mesh and boundary conditions associated with the wave spring validation tests under fully bonded boundary conditions between the separator and surrounding layers. A zoomed in mesh is shown of the separator, sapphire, and wave spring regions since the wave spring is modeled as 10 times the thickness as that of the separator and sapphire (to enforce a constant stiffness over the deformation range of interest). The inner $1/10^{\text{th}}$ of the radius is cut out from both blocks to prevent the need for tetrahedral elements or wedge elements. The orange dashed line schematically represents the locus of points for which $r = 0$. An initial stress is applied to the top of the wave spring at 300 C; once reached, the boundary condition is switched to a zero velocity boundary condition as the temperature is ramped at 5 C per minute through the electrolyte melting transition.

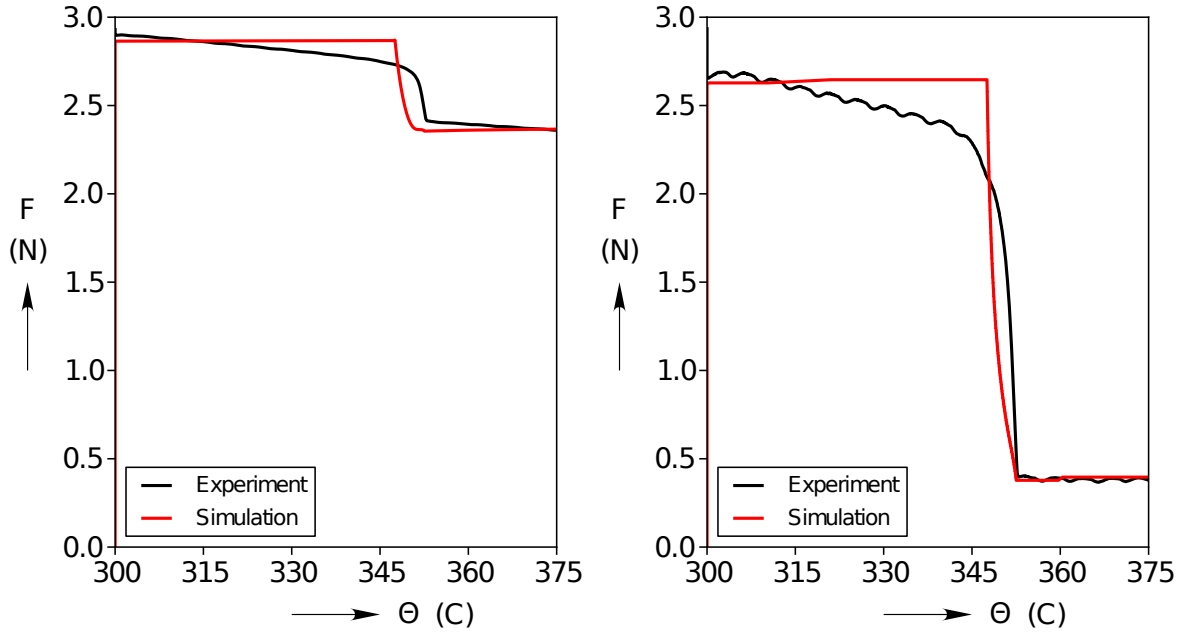

(a) CM06S17 Wave spring test and model prediction ($p = 1$) under bonded conditions

(b) CM08S17 Wave spring test and model prediction ($p = 1$) under bonded conditions

Figure 7.6. Wave spring validation test results and predictions for the case of a perfect bond between the separator, steel platen, and sapphire plate

Chapter 8

Conclusions and Future Directions

We have developed a thermal-mechanical constitutive model for pressed pellet materials designed to capture the volume and shape change behavior as such materials are heated (or cooled) across the melt transition of one of their constituents, the electrolyte. Such a model is relevant for use in molten salt batteries where substantial deformation of the separator layers within the battery are observed during the rise time of the battery (due electrolyte melting and loss of void space in those layers). A suite of characterization experiments are presented that depict solid-like behavior at the macroscale of separator pellets except within the immediately vicinity of the melt transition, about which substantial shape and volume change are observed that depend on the stress-state of the material.

The experiments and model are under electrolyte flow-free conditions. That is, once melted, the electrolyte is confined to remain within the separator pellet as it compacts. Hence, the model represents the combined behavior of the binder, void, and electrolyte in both the solid and liquid states of the latter phase. This approach allows for a straightforward application of experimental data to characterize the thermal, phase-change, and mechanical behaviors of the separator pellet material. Pressure-saturation is not considered here, partly because the development of the model has preceded the porous flow capabilities within the Sierra code suite. However, we intend to integrate this model into a poromechanics framework through the effective stress method. This constitutes future work as many of the theoretical considerations of this report will require re-interpretation as the model is transitioned from representing the entire macroscale material to just representing the binder phase skeleton. However, one advantage of the current framework is that it properly account for electrolyte swelling in its molten state (relative to its solid state), so the change in volume due to electrolyte transport is a natural capability of the model.

Under the assumptions here, the model reasonably calibrates to the experimental data presented and validates against separate wave spring tests that represent battery-like (spring-like) boundary conditions. Boundary conditions between the separator and surrounding layers are not known, but it is found from simulations in this report that once a set of boundary conditions are assumed, for which frictionless and fully-bonded extremes are considered, then the model is able to reasonably fit the characterization (dead-load experiments) and predict the validation (spring-like) experiments. These validation efforts suggest the model is sufficiently robust to describe the mechanics of such materials, but the importance of boundary conditions cannot be determined from these tests, and future experiments are needed to examine this topic.

Theoretically, both the volumetric and isochoric deformation representations can be improved. Currently, volumetric deformation arises through thermal expansion, the loss of pore space, and the specific volume change of the electrolyte. There may also be a volume change of the binder skeleton during the electrolyte melt transition and concomitant binder phase rearrangement. This possibility is possible

References

[1] Moran B., Ortiz M., and Shih C.F. Formulation of implicit finite element methods for multiplicative finite deformation plasticity. *International Journal for Numerical Methods in Engineering*, 29:483–514, 1990.

[2] Paul Butler, Cliff Wagner, Ronald Guidotti, and Imelda Francis. Long-life, multi-tap thermal battery development. *Journal of Power Sources*, 136:240–245, 2004.

[3] Smalley Spring Company. Metric wave springs, October 2013.

[4] Roditi International Corp. Sapphire elastic constansts thermal properties, 2013.

[5] Olivier Coussy. *Mechanics and Physics of Porous Solids*. Wiley, 2010.

[6] Anne Grillet, Lisa Mondy, and Christine Roberts. Experimental characterization of thermal battery component mechanical properties. Memo, Sandia National Laboratories, Sandia National Laboratories Albuquerque, New Mexico 87185 and Livermore, California 94550, 2012.

[7] Ronald A. Guidotti and Patrick Masset. Thermally activated (”thermal”) battery technology part i: An overview. *Journal of Power Sources*, 161:1443–1449, 2006.

[8] Ronald A. Guidotti and Frederick W. Reinhardt. Characterizationof mgo powders for use in thermal batteries. SAND Report 90-2104, Sandia National Laboratories, Sandia National Laboratories Albuquerque, New Mexico 87185 and Livermore, California 94550, 1996.

[9] Ronald A. Guidotti, Frederick W. Reinhardt, and Arthur H. Andazola. Blending study of mgo-based separator materialsfor thermal batteries. Sand report, Sandia National Laboratories, Sandia National Laboratories Albuquerque, New Mexico 87185 and Livermore, California 94550, 2002.

[10] Ronald A. Guidotti, Frederick W. Reinhardt, and Edward V. Thomas. Deformation study of separator pellets for thermal batteries. Sand report, Sandia National Laboratories, Sandia National Laboratories Albuquerque, New Mexico 87185-5800, 1995.

[11] Gerhard A. Holzapfel. *Nonlinear Solid Mechanics*. John Wiley and Sons Ltd., 2001.

[12] George J. Janz. Thermodynamic and transport properties for molten salts: Correlation equations for critically evaluated density, surface tension, electrical conductance, and viscosity data. *Journal of Physical and Chemical Reference Data*, 17(2):1–310, 1988.

[13] Hemrick J.G. and Lara-Curzio E. Characterization of min-k te-1400 thermal insulation. Ornl/tm-2008/089, Oak Ridge National Laboratories, 2008.

[14] Patrick Masset, Serge Schoeffert, Jean-Yves Poinso, and Jean-Claude Poignet. Retained molten salt electrolytes in thermal batteries. *Journal of Power Sources*, 139:356–365, 2005.

[15] MatWeb. Properties of 304 stainless steel, October 2013.

[16] Lisa Mondy. State of knowledge 1/12/2012 electrolyte and powder properties. Memo, Sandia National Laboratories, 2012.

[17] Lisa Mondy, Carlton Brooks, Scott Broome, Steve Bauer, Anne Grillet, Jonathan Rath, Christine Roberts, and Mark Stavig. Experimental characterization of thermal battery separator mechanical properties. Memo, Sandia National Laboratories, Sandia National Laboratories Albuquerque, New Mexico 87185 and Livermore, California 94550, 2012.

[18] David Moore. Acoustic room temperature measurements the elastic constants of the licl-kcl-mgo thermal battery separator pellet. April 2013.

[19] A. Mota, Waiching Sun, Jakob Ostien, James W. Foulk III, and K.N. Long. Lie-group interpolation and variational recovery for internal variables. *Computational Mechanics*, DOI 10.1007/s00466-013-0876-1, 2013.

[20] R.K. Quinn, A.R. Baldwin, J.R. Armijo, P.G. Neiswander, and D.E. Zurawski. Development of a lithium alloy/iron disulfide go-minute primary thermalbattery. Sand report, Sandia National Laboratories, Albuquerque, New Mexico 87185 and Livermore, California 94550, 1979.

[21] Sandia National Laboratories. *CUBIT Geometry and Mesh Generation Toolkit User Documentation*, 14.0 edition, October 2013.

[22] Belytschko T., Liu W.K., and Moran B. *Nonlinear Finite Elements for Continua and Structures*. John Wiley and Sons Ltd., 1 edition, 2001.

[23] Sierra Solid Mechanics Code Team. *Sierra/SolidMechanics 4.28 User's Guide*. Sandia National Laboratories, 4.28 edition, 2013.

Appendix A

Mass, Momentum, and Energy Balances

For completeness, we briefly state the balance laws as necessary to determine the equations of motion for the material. The balance of mass at a material point relates the density in the current (ρ) and reference (ρ_0) configurations to the associated volume ratio (J),

$$\frac{V}{V_0} = \frac{\rho_0}{\rho} = J. \tag{A.1}$$

Typically, the reference state density is the density of the separator material at room temperature. Next, we state the linear momentum and consider a quasi-static setting in which inertial effects are ignored. The local balance of linear momentum in the current configuration at a material point is,

$$\frac{\partial \boldsymbol{\sigma}}{\partial \boldsymbol{x}} + \boldsymbol{b} = \mathbf{0}, \tag{A.2}$$

where $\boldsymbol{\sigma}$ and $\boldsymbol{b}$ represent the Cauchy stress and body force vector defined per unit spatial volume. We do not consider micro polar moments (REFERENCE), and so the balance of angular momentum requires that ($\boldsymbol{\sigma} = \boldsymbol{\sigma}^T$). We will perform calculations in the reference configuration, so we define two useful stress measures, the First and Second Piola-Kirchoff stresses, which are work conjugate to the material time derivatives of the deformation gradient and Green-Lagrange strain respectively,

$$P_{ik} = J\sigma_{ij}F^{-1}_{kj}, \qquad S^{\Gamma}_{ij} = JF^{-1}_{ij}\sigma_{jk}F^{-1}_{lk}, \qquad \Gamma_{ik} = \frac{1}{2}(F_{ji}F_{jk} - \delta_{ik}). \tag{A.3}$$

Here, Γ has been used so as not to confuse the Green-Lagrange strain and the total energy, which we turn our attention to next.

We treat the body as a homogenous, single component material. Neglecting kinetic energy, the time derivative of the total energy in the body is composed of two quantities: the rate of mechanical work the body does against its surroundings and the rate of thermal energy flowing into or generated within the body. When the separator material is in the hot state, and the battery is delivering power, ions are transported through the separator material, which indicates that the rate

of change of the total energy should also include species transport. At this time, we neglect electrochemical potential effects of species transport through the separator material, and we attribute any Joule heating effects within the thermal source term.

Consider a subregion of the body in the reference configuration, denoted $\omega_0 \subset \Omega_0$, with its boundary $\partial\omega_0$. The rate of change of the total internal energy in this region is,

$$\dot{\int_{\omega_0} \varepsilon_0 dV} = -\int_{\partial\omega_0} Q_i N_i dA + \int_{\omega_0} Q dV + \int_{\partial\omega_0} P_{ij} N_j v_i dA + \int_{\omega_0} J b_i v_i dV. \tag{A.4}$$

Here, Q_i and Q represent the referential thermal flux vector (energy per area time) and thermal source (energy per volume time). Employing the divergence theorem, the time-invariance of the reference configuration, and the fact the size of the subregion can be made arbitrarily small, the local form of the energy balance is,

$$\dot{\varepsilon}_0 = -\frac{\partial Q_k}{\partial X_k} + Q + P_{ij}\dot{F}_{ij} = -\frac{\partial Q_k}{\partial X_k} + Q + S^{\Gamma}_{ij}\dot{\Gamma}_{ij}, \tag{A.5}$$

wherein we have used the fact that the mechanical stress power can be written equivalently in terms of the Second Piola-Kirchoff stress and the Green-Lagrange strain.

Appendix B

Entropy Production Inequality

We examine the Second Law of thermodynamics in the form of the Clausius-Duhem inequality within a referential subregion of the body,

$$\int_{\omega_0} \dot{\eta}_0 dV + \int_{\partial\omega_0} \frac{Q_i N_i}{\Theta} dA - \int_{\omega_0} \frac{Q}{\Theta} dV \geq 0, \tag{B.1}$$

wherein we define the referential entropy density, η_0, with units of energy per volume, temperature. Here we define the absolute temperature, Θ, which we require be greater than zero. The local form of Eq. B.1 may be derived following similar arguments as above,

$$\dot{\eta}_0 - \frac{Q}{\Theta} + \frac{1}{\Theta}\frac{\partial Q_i}{\partial \boldsymbol{X}} - \frac{Q_k}{\Theta^2}\frac{\partial \Theta}{\partial X_k} \geq 0 \tag{B.2}$$

By combining the local forms of the energy balance (Eq. A.5) and the entropy production inequality (Eq. B.2) through the elimination of heat source, Q, and multiplication of all terms by Θ, we arrive at,

$$\Theta\dot{\eta}_0 - \dot{\varepsilon}_0 + S^{\Gamma}_{ij}\dot{\Gamma}_{ij} - \frac{Q_k}{\Theta}\frac{\partial \Theta}{\partial X_k} \geq 0 \tag{B.3}$$

The natural thermodynamic state variables for the internal energy density are the entropy density and deformation gradient, so we introduce the Helmholtz free energy density (per unit reference volume) through the standard Legendre transform below since its natural thermodynamic state variables are temperature and deformation gradient,

$$\Psi = \varepsilon_0 - \Theta\eta_0. \tag{B.4}$$

Taking the material time derivative of Eq. B.4 and substituting the result into Eq. B.3 with some additional manipulation, we arrive at the principal inequality of rational mechanics (PIRM) (Coleman and Gurtin 1967) for thermal-mechanical materials,

$$\dot{\Psi} + \eta_0\dot{\Theta} - S^{\Gamma}_{ij}\dot{\Gamma}_{ij} + \frac{Q_k}{\Theta}\frac{\partial \Theta}{\partial X_k} \leq 0. \tag{B.5}$$

Eq. B.7 is also known as the free energy imbalance (Gurtin *et al.* 2010), and it shows that the time evolution of thermodynamic state variables occurs in the direction that minimizes the free energy.

To make further progress with the balance laws and PIRM, we assume *apriori* that the Helmholtz free energy is function of the Green-Lagrange strain (Γ_{ij}), absolute temperature (Θ), and a list of internal state variables ($\{Z^\beta\}$), which are not necessarily thermodynamic state variables. Consequently, the material time derivative of the Helmholtz free energy density (per unit reference volume) in the reference configuration is,

$$\dot{\Psi} = \frac{\partial \Psi}{\partial \Gamma_{ij}} \dot{\Gamma}_{ij} + \frac{\partial \Psi}{\partial \Theta} \dot{\Theta} + \sum_\beta \left(\frac{\partial \Psi}{\partial Z^\beta} \dot{Z^\beta} \right). \tag{B.6}$$

Following the Coleman and Noll procedure (COLEMAN AND NOLL CITATION) we insert Eq. B.6 into the PIRM (Eq. B.7), and pair up terms,

$$\left(\frac{\partial \Psi}{\partial \Gamma_{ij}} - S^\Gamma_{ij} \right) \dot{\Gamma}_{ij} + \left(\eta_0 + \frac{\partial \Psi}{\partial \Theta} \right) \dot{\Theta} + \frac{Q_k}{\Theta} \frac{\partial \Theta}{\partial X_k} + \sum_\beta \left(\frac{\partial \Psi}{\partial Z^\beta} \dot{Z^\beta} \right) \leq 0. \tag{B.7}$$

Because the Green-Lagrange strain, temperature, heat flux, and internal variables may vary independently in an arbitrary thermodynamic process, we are restricted to define the stress and entropy density as,

$$S^\Gamma_{ij} = \frac{\partial \Psi}{\partial \Gamma_{ij}}, \qquad \eta_0 = -\frac{\partial \Psi}{\partial \Theta}. \tag{B.8}$$

To satisfy the PIRM, we further require that,

$$\sum_\beta \left(\frac{\partial \Psi}{\partial Z_\beta} \dot{Z}_\beta \right) \leq 0, \qquad \frac{Q_k}{\Theta} \frac{\partial \Theta}{\partial X_k} \leq 0, \tag{B.9}$$

which mandates that the evolutions of internal variables as well as the transport of thermal energy produce entropy.

DISTRIBUTION:

1	MS	0346	Anne Grillet, 1512
1	MS	0346	Lisa A. Mondy, 1512
1	MS	0346	Christine C. Roberts, 1512
1	MS	0346	Melissa Soehnel, 1512
1	MS	0828	Mario J. Martinez, 1513
1	MS	0828	Jonathan Clausen, 1513
1	MS	0836	Scott A. Roberts, 1514
1	MS	0840	Huei Eliot Fang, 1554
1	MS	0840	Kevin N. Long, 1554
1	MS	0840	William M. Scherzinger, 1554
1	MS	0840	Benjamin Reedlun, 1554
1	MS	0840	Pania Newell, 1554
1	MS	0840	John Pott, 1555
1	MS	0346	Diane E. Peebles, 1526
1	MS	0613	David Ingersoll, 2546
1	MS	0613	Thomas F. Wunsch, 2546
1	MS	0614	Daniel E. Wesolowskil, 2545
1	MS	0614	Steven K. Showalter, 2547
1	MS	0614	Eric D. Branson, 2547
1	MS	0613	Dennis K. Wong, 2548
1	MS	0899	Technical Library, 9536

Sandia National Laboratories